Magnetically modified spherical accretion in GRMHD: reconnection-driven convection and jet propagation

S. M. Ressler,[1]★ E. Quataert,[2,3] C. J. White[3] and O. Blaes [●][4]

[1]*Kavli Institute for Theoretical Physics, University of California Santa Barbara, Santa Barbara, CA 93107, USA*
[2]*Departments of Astronomy & Physics, Theoretical Astrophysics Center, University of California, Berkeley, CA 94720, USA*
[3]*Department of Astrophysical Sciences, Princeton University, Princeton, NJ 08544, USA*
[4]*Department of Physics,University of California, Santa Barbara, CA 93106, USA*

ABSTRACT

We present 3D general relativistic magnetohydrodynamic simulations of zero angular momentum accretion around a rapidly rotating black hole, modified by the presence of initially uniform magnetic fields. We consider several angles between the magnetic field direction and the black hole spin. In the resulting flows, the mid-plane dynamics are governed by magnetic reconnection-driven turbulence in a magnetically arrested (or a nearly arrested) state. Electromagnetic jets with outflow efficiencies ∼10–200 per cent occupy the polar regions, reaching several hundred gravitational radii before they dissipate due to the kink instability. The jet directions fluctuate in time and can be tilted by as much as ∼30° with respect to black hole spin, but this tilt does not depend strongly on the tilt of the initial magnetic field. A jet forms even when there is no initial net vertical magnetic flux since turbulent, horizon-scale fluctuations can generate a net vertical field locally. Peak jet power is obtained for an initial magnetic field tilted by 40°–80° with respect to the black hole spin because this maximizes the amount of magnetic flux that can reach the black hole. These simulations may be a reasonable model for low luminosity black hole accretion flows such as Sgr A* or M87.

Key words: accretion, accretion discs – black hole physics – convection – magnetic reconnection – MHD – Galaxy: centre.

1 INTRODUCTION

Well-resolved, 3D general relativistic magnetohydrodynamic (GRMHD) simulations of accreting black holes are now commonplace (De Villiers & Hawley 2003; Gammie, McKinney & Tóth 2003; White, Stone & Gammie 2016; Porth et al. 2017; Liska et al. 2019a) and are frequently used to model low luminosity accretion flows such as those surrounding the supermassive black holes Sagittarius A* (Sgr A*) and the one at the centre of M87 (Mościbrodzka et al. 2009; Chan et al. 2015; Mościbrodzka, Falcke & Shiokawa 2016; Chael, Narayan & Johnson 2019; Event Horizon Telescope Collaboration 2019b; Dexter et al. 2020a). The most common strategy is to initialize the simulations with a torus in hydrodynamic equilibrium (e.g. Fishbone & Moncrief 1976; Penna, Kulkarni & Narayan 2013) and add a dynamically unimportant magnetic field to seed the magnetorotational instability (MRI; Balbus & Hawley 1991) and drive accretion. By varying the size of the torus, the initial magnetic field geometry, and the magnitude of the black hole spin, a relatively diverse set of solutions emerge that can, in principle, be used to constrain properties of observed systems. In order to do so precisely, one must understand not only the dependence of the results on these particular parameters, but also on the assumptions that go into each model.

For instance, much recent work has been devoted to exploring the effects of non-ideal physics expected to be important for low

luminosity accretion flows. This includes two-temperature effects (Ressler et al. 2015; Sądowski et al. 2017; Chael et al. 2018), non-thermal electron acceleration (Ball et al. 2016; Chael, Narayan & Sądowski 2017; Mao, Dexter & Quataert 2017), radiation (Ryan, Dolence & Gammie 2015; Ryan et al. 2017; Sądowski et al. 2017; Chael et al. 2019), magnetic resistivity (Ripperda et al. 2019), and anisotropic conduction/viscosity (Chandra, Foucart & Gammie 2017; Foucart et al. 2017). These works build on earlier 1D semi-analytic models that more easily incorporated extra physics (e.g. Narayan & Yi 1995; Özel, Psaltis & Narayan 2000; Yuan, Quataert & Narayan 2003; Johnson & Quataert 2007). Another active research frontier is that of tilted accretion discs, where the spin of the black hole is misaligned with the angular momentum of the flow (Fragile et al. 2007; Liska et al. 2018, 2019b; White, Quataert & Blaes 2019b; Liska et al. 2020a). Tilted discs not only have different dynamics than non-tilted discs (e.g. precession, standing shocks), they can also produce qualitatively different images/spectra (e.g. ellipsoidal morphologies, larger image size; Chatterjee et al. 2020; White et al. 2020).

Less explored are the effects of the torus initial conditions. This was the motivation for a series of multiscale simulations of Sgr A* (Ressler, Quataert & Stone 2018, 2020a; Ressler et al. 2020b, building on earlier work by Cuadra et al. 2005, 2006; Cuadra, Nayakshin & Martins 2008, see also Calderón et al. 2020) that used observationally constrained Wolf–Rayet stellar wind source terms in order to essentially eliminate the need for assumed initial conditions. Two of the key findings of these studies were that the gas ultimately reaching the horizon had (1) a relatively small amount of angular

★ E-mail: seanmressler@gmail.com

momentum and (2) a relatively large amount of coherent magnetic flux. As a consequence, the MRI had little effect on the dynamics and the flow became magnetically arrested (Igumenshchev, Narayan & Abramowicz 2003; Narayan, Igumenshchev & Abramowicz 2003) on horizon scales (at least for $a = 0$, where a is the dimensionless spin of the black hole). Although we do not typically have such intricate knowledge of the stellar/gas population surrounding supermassive black holes in other galaxies, it is not unreasonable to assume that some fraction of these objects are fed in a similar way.

In this work, we seek to investigate an alternative model of low angular momentum, magnetized accretion flows in GRMHD. In particular, we consider the limiting case of a non-rotating flow at large radii with an initially uniform magnetic field, the MHD analogue of the classic force-free Wald (1974) and Bicak & Janis (1985) solutions. In non-relativistic simulations (Igumenshchev & Narayan 2002; Pen, Matzner & Wong 2003; Pang et al. 2011), such flows have been shown to have distinct characteristics from those with significant angular momentum, e.g. turbulence driven by magnetic reconnection and nearly hydrostatic force balance. For a non-spinning black hole, the qualitative nature of these solutions likely carries over to full GRMHD, though with order unity quantitative corrections near the horizon. Conversely, for a rapidly spinning black hole, the large supply of coherent magnetic flux will presumably drive a Blandford & Znajek (1977) jet that would back-react on the quasi-spherical inflow and could significantly alter the resulting dynamics. Additionally, frame dragging and magnetic torque could lead to non-negligible azimuthal velocities near the horizon even if there is initially no rotation.

One potentially important parameter in these simulations is the angle that the initial magnetic field makes with the black hole spin axis. Previous works that study tilt have used equilibrium tori seeded with various magnetic field geometries contained within those tori (e.g. Fragile et al. 2007; Liska et al. 2018, 2019b; White et al. 2019b; Liska et al. 2020a). This means that the orientation of the magnetic field was tilted along with the angular momentum of the gas, making it hard to disentangle the effects of magnetic tilt versus angular momentum tilt. Here, starting with no angular momentum, we can investigate the magnetic tilt in isolation in order to determine how much, if any, it effects the orientation of both the jet and the accretion flow. In particular, we focus on four magnetic tilt angles, $0°$, $30°$, $60°$, and $90°$, with an initial plasma β of 100, a Bondi radius of 200 gravitational radii, and a dimensionless black hole spin $a = 0.9375$.

This work proceeds as follows. Section 2 outlines the initial conditions and numerical model, Section 3 presents the resulting simulations, Section 4 analyses further one particular simulation that is an outlier from the rest, Section 5 discusses the dependence of our results on various parameters, Section 6 compares these results to previous work, and Section 7 concludes.

2 MODEL

Since non-radiative GRMHD simulations are scale-free, we will generally use length and time units that scale with the mass of the black hole and set the speed of light, c, and the gravitational constant, G, equal to unity. Thus, in these units, the mass of the black hole, M, is our standard unit for both length and time, though we often use the gravitational radii $r_g = M$ as an equivalent notation.

Our simulations are carried out in `Athena++` (White et al. 2016; Stone et al. 2020), a 3D grid-based code that solves the equations of conservative GRMHD in Cartesian Kerr–Schild coordinates (CKS; Kerr 1963). These relate to the spherical Kerr–Schild r, θ, φ

coordinates via

$$x = r \sin(\theta) \cos(\varphi) + a \sin(\theta) \sin(\varphi),$$
$$y = r \sin(\theta) \sin(\varphi) - a \sin(\theta) \cos(\varphi),$$
$$z = r \cos(\theta), \tag{1}$$

where a is the dimensionless spin of the black hole. Our computational domain is a rectangular box of size $3200r_g \times 3200r_g \times 25600r_g$ with base resolution $24 \times 24 \times 192$ cells in the x-, y-, and z-directions. The box is larger in the z-direction in order to ensure that any relativistic jet that might form does not interact with the outer boundary. We use an additional 12 levels of nested static mesh refinement (SMR) to achieve approximately logarithmic spacing in r, using meshblocks of size $12 \times 24 \times 16$ cells. The outer boundary of the first level is located at $|z| = 6400r_g$ and $|x|$, $|y| = 1600r_g$, while the outer boundary of the second level is located at $|z| = 3200r_g$ and $|x|$, $|y| = 1600r_g$. The outer boundaries for the remaining $n \geq 3$ levels are located at $|x|$, $|y|$, $|z| = 1600/2^{n-3} r_g$. The finest grid spacing is achieved for $|x|$, $|y|$, $|z| < 3.125r_g$, where Δx, Δy, $\Delta z \approx 0.0326r_g$, ensuring that the event horizon is well resolved since $(\Delta x, \Delta y, \Delta z)/r_H \ll 1$, where $r_H = 1 + \sqrt{1 - a^2}$ is the event horizon radius. All of our simulations use $a = 0.9375$, for which $r_H \approx 1.35r_g$. Note that for $|x|$, $|y|$, $|z| \leq 1600r_g$, the grid is equivalent to a $(1600r_g)^3$ box with a 192^3 base resolution with nine levels of extra mesh refinement. Our resolution is comparable to or better than the highest resolution (192^3) spherical KS torus simulations presented in the Event Horizon Telescope (EHT) code comparison project that were found to be converged (Porth et al. 2019). Specifically, at $(r = 12r_g, \theta = \pi/2)$, our simulations are better resolved by almost a factor of 2 in the radial direction and more than a factor of 2.5 in the φ direction, while having a comparable resolution in the θ direction to the most mid-plane refined of their simulations.

The initial conditions for these simulations are inspired by previous non-relativistic models of magnetically modified spherical accretion in the literature (e.g. Igumenshchev & Narayan 2002; Pen et al. 2003; Pang et al. 2011). Outside $r = 6r_g$, we start with a uniform density, $\rho_0 = 1$, and uniform pressure, P_0, such that the Bondi radius is $r_B \equiv 2M/c_{s,0}^2 = 200M$, where $c_{s,0} = \sqrt{\gamma P_0/\rho_0}$ is the non-relativistic, adiabatic sound speed. These non-relativistic expressions are appropriate for large Bondi radii where general relativistic effects are small. For simplicity, the gas is stationary, with the spatial components of the four-velocity set to zero. Inside $r = 6r_g$, the density and pressure are set to the numerical floors and again the spatial components of the four-velocity are set to zero. We set the initial magnetic field by taking the curl of a vector potential A_μ:

$$B^i = \frac{1}{\sqrt{-g}} \epsilon^{ijk} \frac{\partial}{\partial x^j} A_k, \tag{2}$$

where $g = -1$ is the determinant of the CKS metric and ϵ^{ijk} is the Levi–Cevita symbol. All spatial components of A_μ are zero except for the y-component (note that the t-component is irrelevant), which we set to be $A_y \propto e^{5(1 - 6/r)}[-z \sin(\psi) + x \cos(\psi)]$, with the normalization set such that $\beta \equiv P/P_B = 100$ at large radii, where $P_B = b^2/2$ is the magnetic pressure, $b^2 = b^\mu b_\mu$, and b^μ is the magnetic field four vector in Lorentz–Heaviside units. This vector potential corresponds to a uniform field that is inclined by an angle of ψ with respect to the black hole spin axis for $r > 6r_g$. For $r \lesssim 6r_g$, the field exponentially decays to zero, meaning that the field lines wrap around $r \approx 6$ as shown in the upper left-hand panels of Figs 1–4.

Inside $r < r_H/2$, we set the density/pressure to the numerical floors and the four-velocity to free-fall. Within this region, the induction equation is solved without alteration. Although CKS coordinates are horizon-penetrating, there is still a coordinate singularity at $z = 0$,
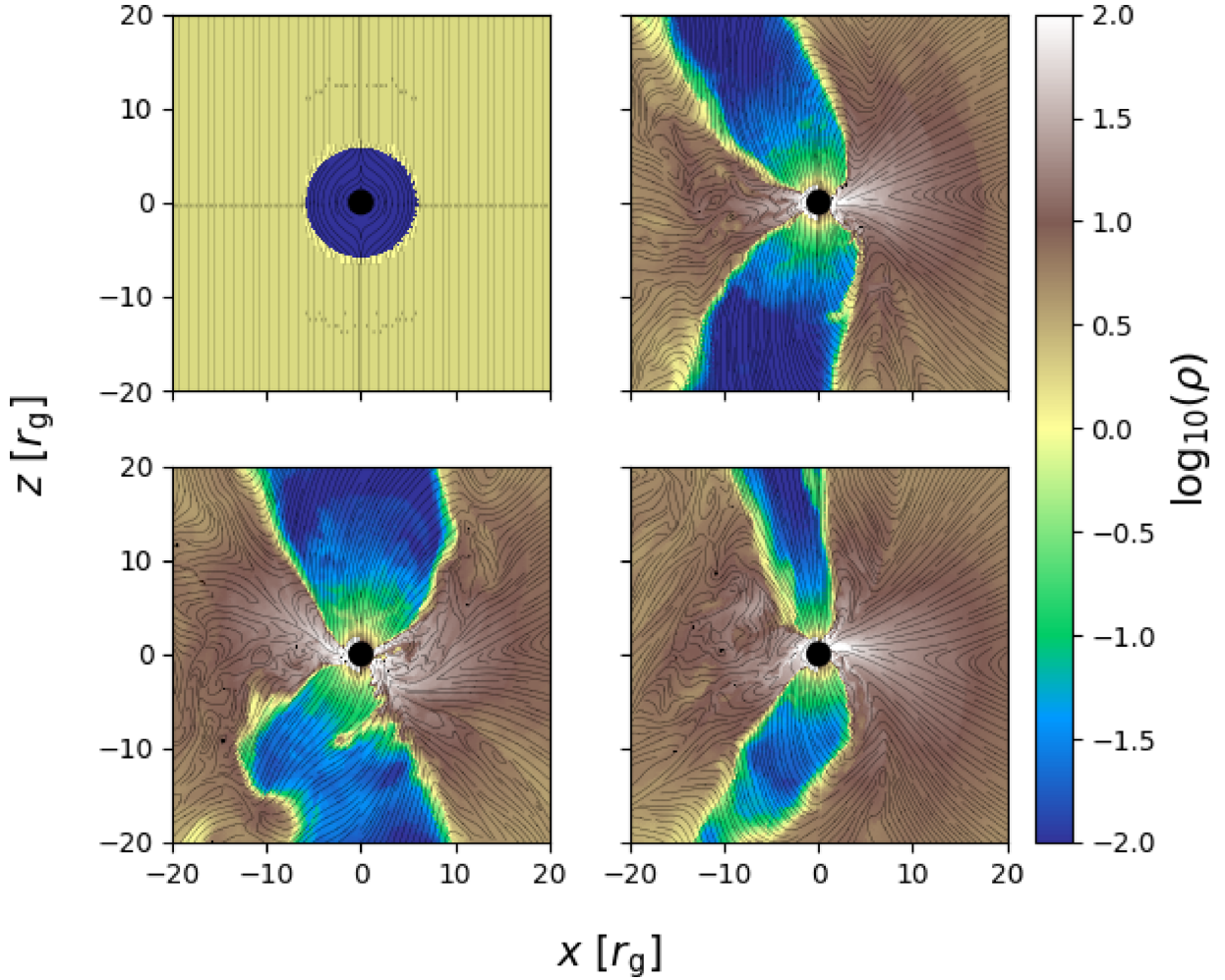
Figure 1. 2D slice through the x–z plane of mass density overplotted with magnetic field lines at four different times in the $\psi = 0°$ simulation. Starting from the top left-hand panel and proceeding clockwise, the panels represent 0, 4000, 10 000, and 18 000 M. The initially uniform field accretes through the event horizon and the rapidly spinning black hole drives a powerful jet. The accreting field also reconnects, heating the gas and driving turbulence.

$\sqrt{x^2 + y^2} = |a|$ (i.e. $r = 0$, $\theta = \pi/2$). To avoid this, for $|z| < 10^{-5} r_g$ we set $z = 10^{-5} r_g$ in the calculation of the metric. Since this is well inside the event horizon, it has no effect on our results. The outer boundary conditions at the box faces are fixed to the initial conditions.

The density floor is $10^{-6}(r/r_g)^{-3/2}$ and the pressure floor is $3.33 \times 10^{-9}(r/r_g)^{-5/2}$, with $\sigma \equiv b^2/\rho \leq 100 = \sigma_{\max}$ and $\beta \geq 0.001$ enforced via additional density and pressure floors, respectively. Here, β is the ratio between the thermal and magnetic pressures. Additionally, the velocity of the gas is limited such that the maximum Lorentz factor is 50 in the CKS normal frame.

We run simulations with $\psi = 0°$, $30°$, $60°$, and $90°$ for 20 000 M, about 10 free-fall times at the Bondi radius.[1] We set the adiabatic index to $\gamma = 5/3$.

Finally, we note that for analysis purposes we will often convert the simulation data from CKS coordinates x, y, and z to spherical KS coordinates r, θ, and φ using the inverse of equation (1). Four vectors are converted using the Jacobian:

$$A^\mu_{(KS)} = \frac{\partial x^\mu_{(KS)}}{\partial x^\nu_{(CKS)}} A^\nu_{(CKS)}. \tag{3}$$

We will also use an orthonomal tetrad to measure local velocities in the zero angular momentum (ZAMO) frame, which we define in Boyer–Lindquist coordinates (Boyer & Lindquist 1967) as an observer with four-velocity

$$\eta^{BL}_\mu = \left(-\frac{1}{\sqrt{-g^{tt}_{BL}}}, 0, 0, 0\right). \tag{4}$$

The corresponding tetrad is

$$e^\mu_{t,BL} = \eta^\mu_{BL},$$

$$e^\mu_{r,BL} = \left(0, \frac{1}{\sqrt{g^{BL}_{rr}}}, 0, 0\right),$$

$$e^\mu_{\theta,BL} = \left(0, 0, \frac{1}{\sqrt{g^{BL}_{\theta\theta}}}, 0\right),$$

$$e^\mu_{\phi,BL} = \left(0, 0, 0, \frac{1}{\sqrt{g^{BL}_{\varphi\varphi}}}\right), \tag{5}$$

---

[1]The $\psi = 90°$ simulation uses a slightly different grid than the other three simulations in that the $|z| > 1600 r_g$ region is excluded. Within $|x|, |y|, |z| < 1600 r_g$, the grids are identical.
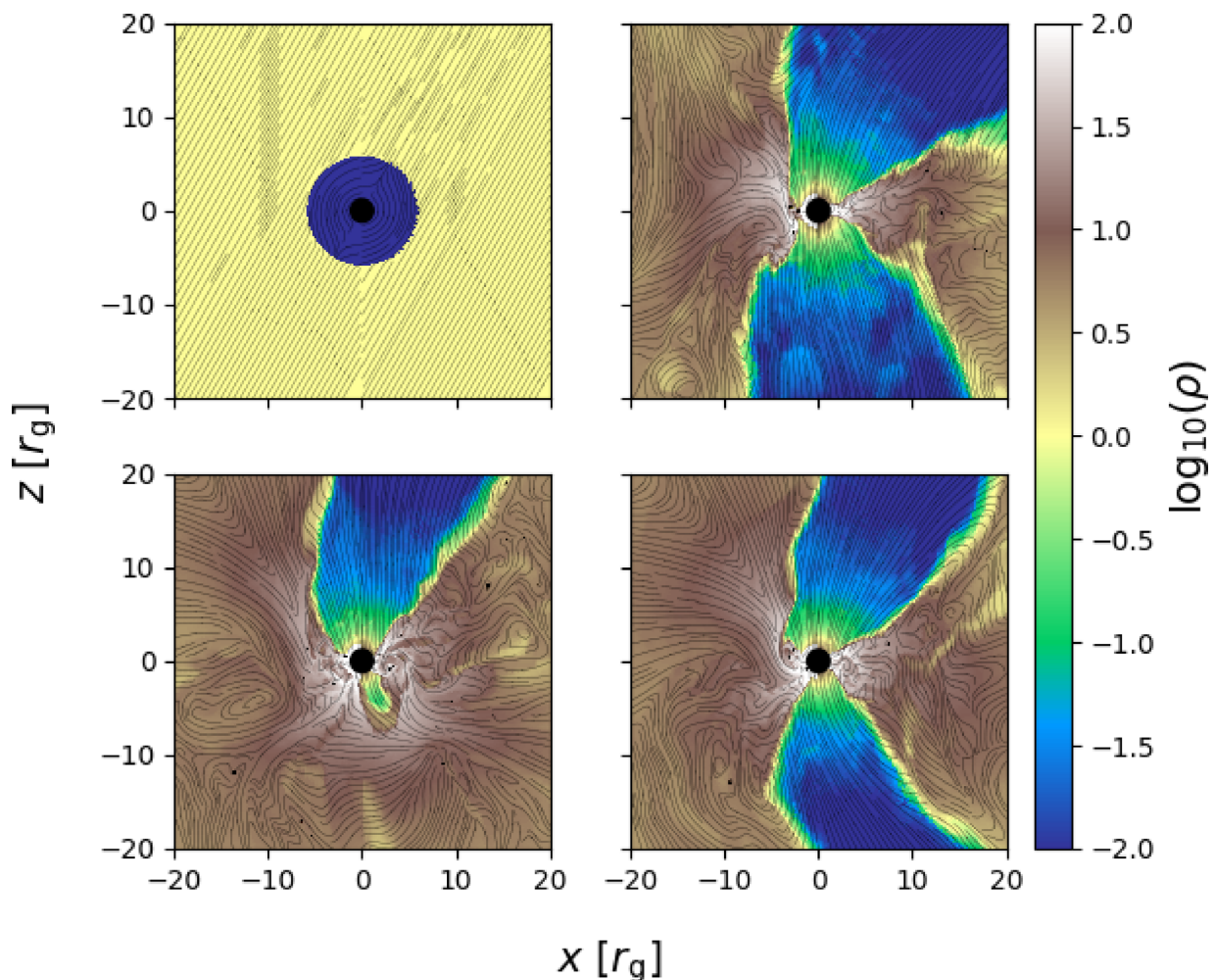
Figure 2. Same as Fig. 1 but for $\psi = 30°$.

so that the physical velocities in the *i*th direction are

$$V^i = \frac{u_{\mathrm{KS}}^\mu e_\mu^{i,\mathrm{KS}}}{u_{\mathrm{KS}}^\mu e_\mu^{t,\mathrm{KS}}}, \tag{6}$$

where $e_{\nu,\mathrm{KS}}^\mu$ is $e_{\nu,\mathrm{BL}}^\mu$ converted to KS coordinates.

3 RESULTS

3.1 Overview

Figs 1–4 show 2D contour slices of the mass density overplotted with magnetic field lines at four different times for our $\psi = 0°$, $30°$, $60°$, and $90°$ simulations, respectively. In all cases, the initially weak magnetic field is dragged inwards with the flow until it becomes dynamically important. Absent black hole spin, this would result in a 'pinched' geometry of the field where matter is pushed away from the magnetic poles and towards the magnetic mid-plane. In non-relativistic MHD, this ultimately leads to a highly disordered state where heating associated with the reconnection of the pinched field drives convection (Igumenshchev & Narayan 2002; Pen et al. 2003; Pang et al. 2011). Here, however, the effects of the rapidly spinning black hole significantly alter this scenario. For $\psi = 0°$, $30°$, and $60°$, the accumulation of flux threading the horizon (particularly flux parallel to the black hole spin) caused by the initially spherical accretion leads to the formation of a magnetically dominated jet by $\sim 2000\,M$ via the Blandford & Znajek (1977) mechanism in which

the magnetic field is tightly wound up in the φ-direction and propels matter/energy outwards. We find that the jet is always aligned with the black hole spin for $r \lesssim 5r_g$, though at larger radii it can be significantly tilted (we discuss jet orientation in more detail in Section 3.3). The strong outflow evacuates the polar regions of matter but leaves a broad distribution of gas in the mid-plane. Turbulence driven by magnetic reconnection is visible at small ($r \lesssim 5r_g$) radii in Figs 1–4.

The $\psi = 90°$ simulation shows similar behaviour between 5000 and 15 000 M but much different behaviour at earlier and later times. Initially, the dynamics are governed by reconnection-driven turbulence with no preferred direction, the GRMHD analogue to the non-relativistic simulations mentioned above. This state persists until turbulent fluctuations spontaneously generate a net locally vertical magnetic field that accretes and powers a jet. However, since this vertical field is not being continuously supplied by gas at large radii, the jet dies off and the convection-dominated state resumes. We expect that if the simulation were to run for a longer time then another turbulently generated, locally vertical field would be created and the cycle would repeat.

The simulations also have interesting azimuthal structure. Fig. 5 shows plasma β in the mid-plane of the $\psi = 30°$ simulation as an example at four different times (the other three simulations display similar contours and are thus not shown). The flow structure is highly non-axisymmetric, with clear spiral structure caused by the rotating space–time of the central Kerr black hole. Such structures are largest and most coherent in the $\psi = 90°$ simulation since the twisting of the
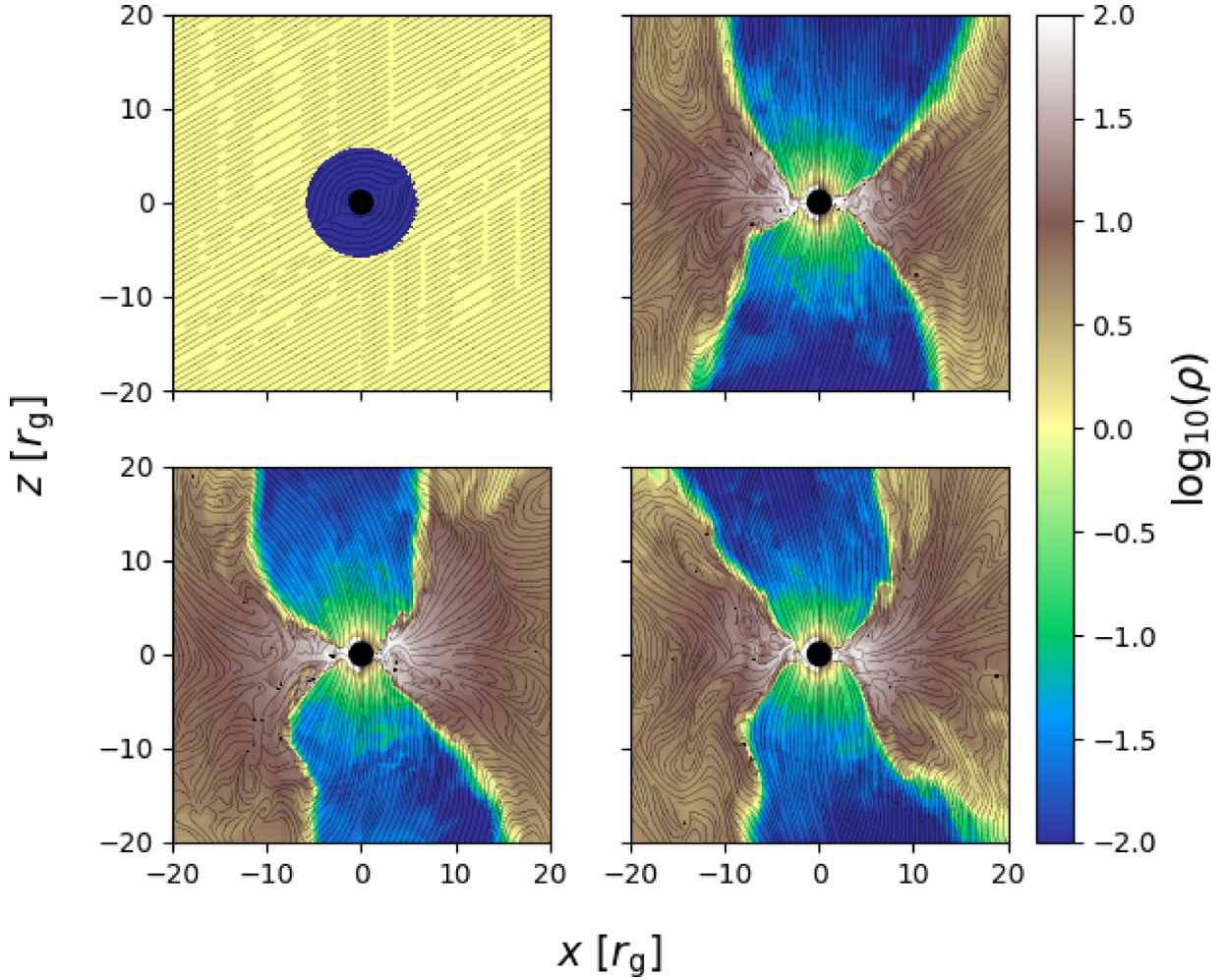
Figure 3. Same as Fig. 1 but for $\psi = 60°$.

initially horizontal field by the black hole provides the most spatially extended torque on the gas. In all cases, matter generally accretes in thin streams with higher β ($\gtrsim 1$) regions surrounded by lower β ($\lesssim 1$) magnetically dominated regions.

Fig. 6 shows time and angle averages of several important quantities for the four simulations during the interval 10000–15000 M. These include the mass density, ρ; the mid-plane angular velocity relative to the prograde Keplerian value measured in the ZAMO frame, V^φ/V_{kep}, where V_{kep} is computed by transforming $\hat{\varphi}^{\text{BL}}_{\text{Kep}} = 1/(r^{3/2} + a)$ to the ZAMO frame; the radial velocity divided by the sound speed measured in the ZAMO frame, V^r/c_s, where $c_s = \sqrt{\gamma P/w}$ and $w = \rho + \gamma/(\gamma - 1)P$; temperature, $T_g = P/\rho$ (assuming ionized hydrogen); entropy, $s = (\gamma - 1)^{-1}\log(P/\rho^\gamma)$; and plasma β. Here, we compute angle averages in KS coordinates by evaluating

$$\langle A \rangle_X = \frac{\iint A X \, \mathrm{d}\Omega}{\iint X \, \mathrm{d}\Omega}, \qquad (7)$$

where $\mathrm{d}\Omega = \sqrt{-g_{\text{KS}}}\mathrm{d}\varphi\mathrm{d}\theta$ and $g_{\text{KS}} = -\sin(\theta)^2[r^2 + a^2\cos(\theta)^2]^2$. The quantities plotted in Fig. 6 are typically mass weighted in order to study the properties of the accreting mid-plane. We will discuss the properties of the jet later in Section 3.3. Qualitatively, the four simulations display the same basic trends in the mass-weighted radial profiles. Within $r \lesssim 10r_g$, the magnetic field has been compressed to

the point that the flow is magnetically dominated, with $\beta \lesssim 1$, providing a Lorentz force strong enough to slow the infall to the degree that the sonic point is located at $\sim 2 \, r_g$ instead of the hydrodynamic Bondi value of $\sim 8.8 \, r_g$.[2] Note, however, that this Lorentz force is still $\lesssim$ the thermal pressure force because the magnetic pressure and tension terms tend to act in opposite directions, reducing the overall net magnetic force on the gas. The strong field is reconnecting and heating the gas, as evidenced by the entropy increasing with decreasing r and the associated temperature increase beyond what one would predict from adiabatic compression alone.[3] Inside the Bondi radius (200 r_g) the mass density settles into an $\rho \propto r^{-1}$ profile. Finally, despite the stationary, spherical initial conditions, the frame-dragging effects of the $a = 0.9375$ black hole on the magnetic field lines torque the gas

---

[2]The hydrodynamic Bondi radius for $a = 0$ is calculated analytically (Michel 1972; Hawley, Smarr & Wilson 1984). We have verified in a 3D hydrodynamic simulation that a spherical flow on to an $a = 0.9375$ black hole has the same sonic point radius.

[3]It is somewhat surprising to see the entropy continue to increase after the fluid passes through the sonic point ($r \lesssim 2r_g$) and plunges through the event horizon at $r \approx 1.35 \, r_g$ because n this narrow radial range one would expect the gas to essentially be experiencing adiabatic free-fall. This may be because (1) averaging effects result in an average radial entropy profile that is not necessarily representative of the entropy profile along individual streamlines or (2) the thermodynamics in this region may be less reliable than at larger radii because $\sigma \gtrsim 1$.
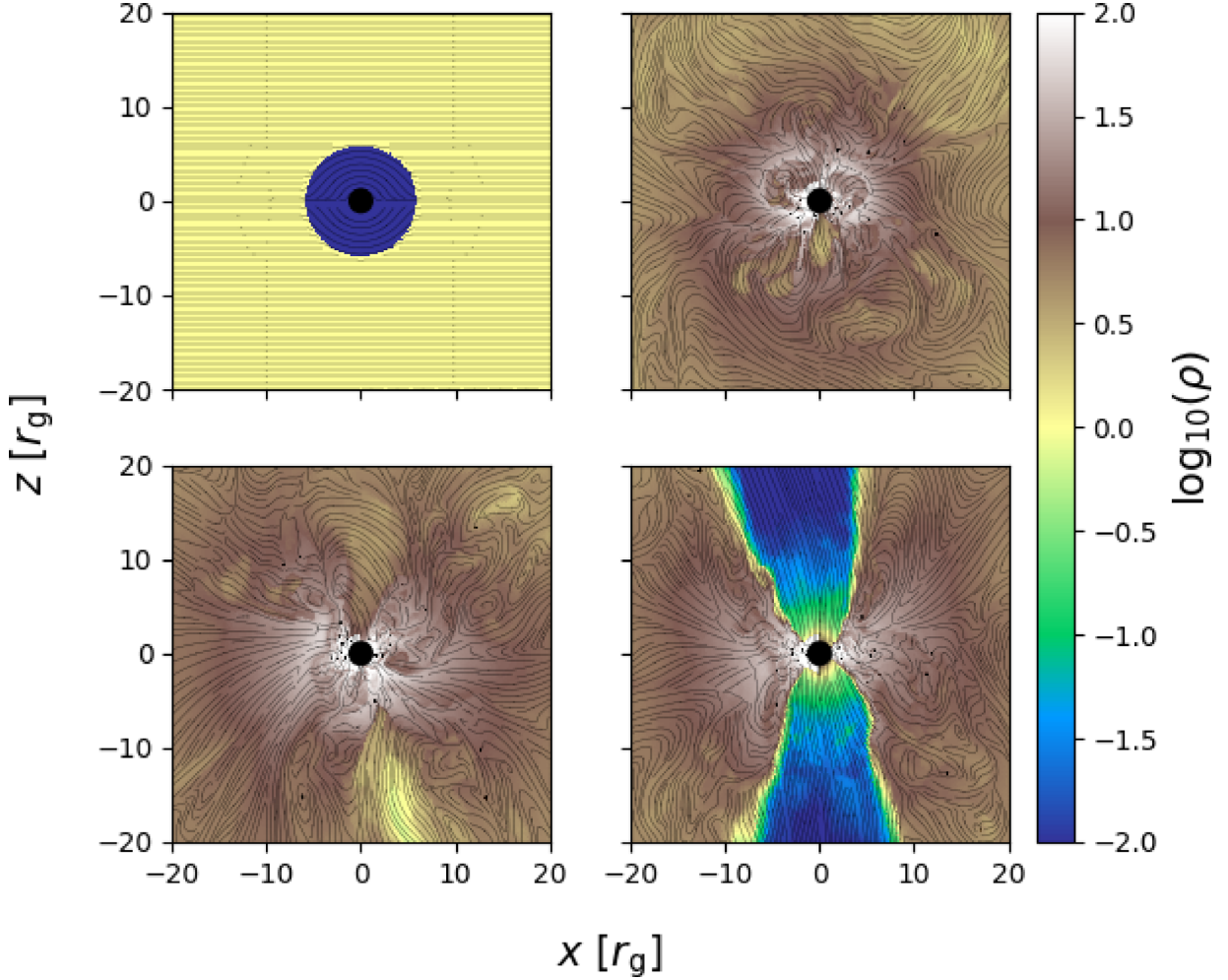
Figure 4. Same as Fig. 1 but for $\psi = 90°$. At 4000 M (top right-hand panel), the gas is in a state of disordered convection that persists until a net vertical magnetic field is randomly generated locally and a jet is formed.

enough to create non-neglible prograde rotational velocities for $r \lesssim$ 20–50 r_g, reaching up to ∼0.5 Keplerian near the horizon. Note that this is indeed a torquing effect in the sense that u_φ is non-zero and u^φ is larger than what one would expect from frame dragging of the gas alone (in which case V^φ would be zero). Compared to the gas in the $\psi = 0°$ and $\psi = 30°$ simulations, the gas in the $\psi = 60°$ and $\psi = 90°$ simulations has a shallower rotation curve for $r \gtrsim 3\,r_g$, meaning that significant angular velocity is present out to slightly larger radii. This is likely because the larger amount of field perpendicular to the spin axis provides a longer 'lever arm' to torque the flow.

The biggest outlier in Fig. 6 is the $\psi = 60°$ simulation, which has a ∼2–3 times slower radial velocity at all radii compared to the other simulations, as well as a ∼2–3 times lower density, a $\lesssim$2 times lower temperature, and a ∼2 times higher P/ρ^γ for $r \lesssim 10\,r_g$. As we will show in the next subsection, this is because the amount of flux able to reach the black hole for $\psi = 60°$ is larger than the other three simulations. We speculate as to why in Section 4.

In terms of energy flux, we find that convection is inefficient at transporting energy outwards. Fig. 7 demonstrates this by plotting the average total flux of energy contained in matter,

$$F_{\rm E,Ma} = -\frac{4\pi}{3}\left(3r^2 + a^2\right)\left\langle\left(1 + \frac{\gamma}{\gamma-1}\frac{P}{\rho}\right)\rho u^r u_t - \rho u^r\right\rangle, \quad (8)$$

compared to the average flux of matter energy through laminar advection,

$$F_{\rm adv,Ma} = -\frac{4\pi}{3}\left(3r^2 + a^2\right)\left\langle\left(1 + \frac{\gamma}{\gamma-1}\frac{P}{\rho}\right)u_t - 1\right\rangle\langle\rho u^r\rangle, \quad (9)$$

and the average convective flux, $F_{\rm conv,Ma} = F_{\rm E,Ma} - F_{\rm adv,Ma}$, for all four simulations. In averaging these terms, we exclude the low density jet by focussing only on $|\theta - \pi/2| < \theta_H$, where $\theta_H = \langle|\theta - \pi/2|\rangle_\rho$ is the half-opening angle of the mass distribution. Energy flows inwards predominantly by laminar advection, while convection provides only a small outward contribution with $|F_{\rm conv,Ma}|$ a factor of 3–10 times smaller than $|F_{\rm adv,Ma}|$ except for $r \lesssim$ a few r_g where the two fluxes can be comparable. The lack of a strong outward convective flux explains why the density profile in Fig. 6 is steeper than the $r^{-1/2}$ predicted by models where convection is the dominant energy transport mechanism (e.g. Narayan, Igumenshchev & Abramowicz 2000; Quataert & Gruzinov 2000; Igumenshchev & Narayan 2002).

3.2 Time evolution

We now turn our attention to the temporal variability of the four simulations. A key quantity in magnetized black hole accretion is the
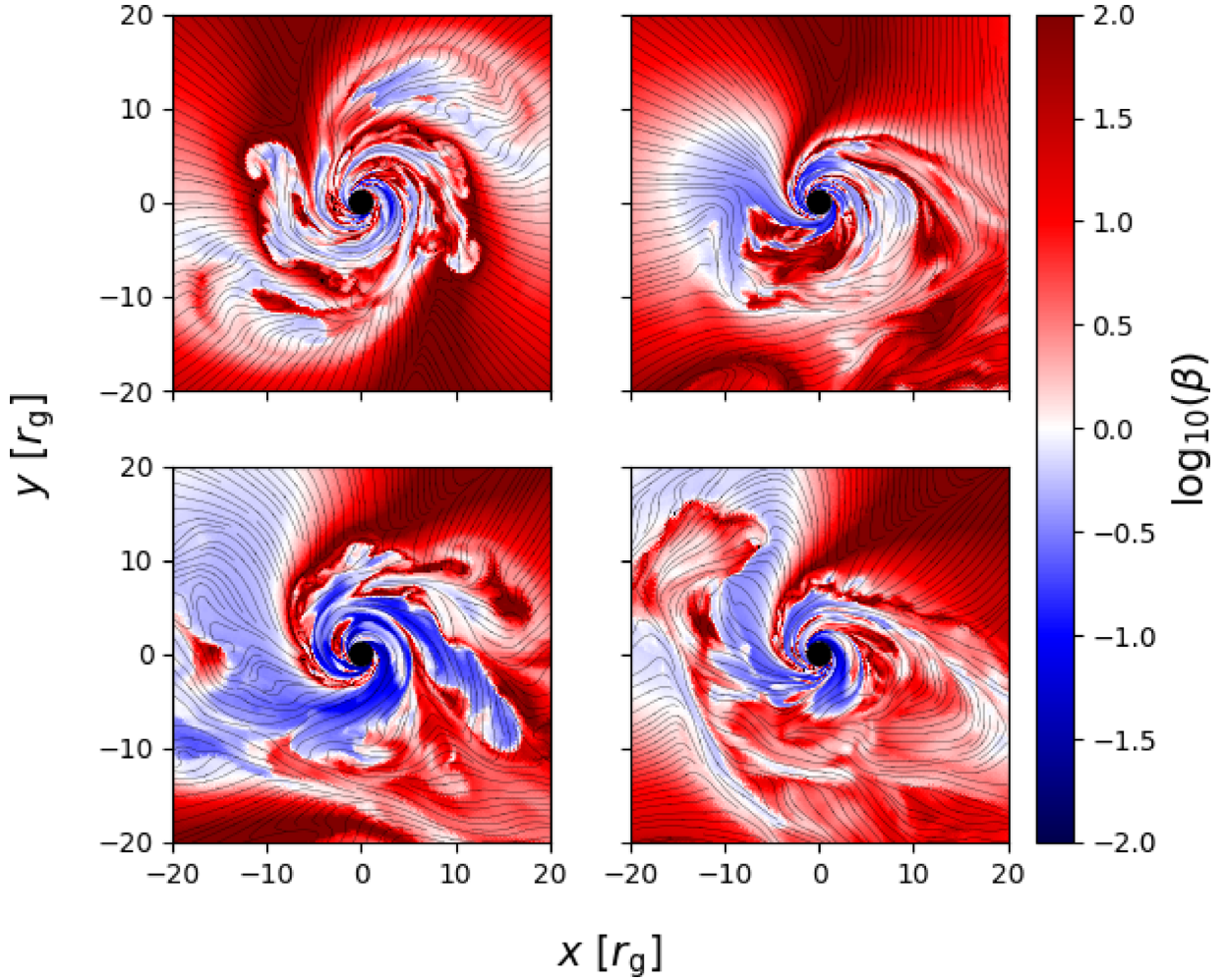
Figure 5. Mid-plane slice of plasma β at four different times in our $\psi = 30°$ simulation overplotted with magnetic field lines. Starting from the top left-hand panel and proceeding clockwise, the panels represent 2000, 8000, 14 000, and 20 000 M. Accretion proceeds along thin, high-density streams surrounded by highly magnetized, low-β regions. Contours of β in the other three simulations look similar.

dimensionless measure of the magnetic flux threading the horizon:

$$\phi_{BH} \equiv \frac{\sqrt{4\pi} \iint |B^r| \mathrm{d}\Omega}{2\sqrt{|\dot{M}|}}, \qquad (10)$$

where B^r is the radial component of the magnetic three-vector and $\dot{M}$ is the accretion rate. In GRMHD torus simulations, this quantity seems to have a maximum possible value at $\phi_{BH} \approx 40$–60 (e.g. Tchekhovskoy, Narayan & McKinney 2011; White, Stone & Quataert 2019a), at which point the flow transitions to the magnetically arrested state where the outwards Lorentz force is strong enough to periodically halt accretion in a highly time-variable configuration (Igumenshchev et al. 2003; Narayan et al. 2003). In the top panel of Fig. 8, we plot ϕ_{BH} for our four simulations. The $\psi = 0°$ curve displays quintessential magnetically arrested disc (MAD) characteristics, with ϕ_{BH} varying between 30 and 60 in periodic cycles of accumulation and dissipation. The accretion rate in the second panel of Fig. 8 varies accordingly (between 0.05 and 0.35 times the Bondi rate) with the peaks in ϕ_{BH} associated with valleys in $\dot{M}$, and vice versa. In contrast, the $\psi = 30°$ simulation does not seem to reach the MAD state, with a saturated ϕ_{BH} of $\sim$30 that is much less variable than the $\psi = 0°$ case. The accretion

rate is also more constant in time than $\psi = 0°$, though the time-averaged values in both simulations are comparable, $\sim$0.2 times the Bondi rate. The $\psi = 90°$ simulation has an even smaller amount of magnetic flux reaching the black hole, $\phi_{BH} \approx 20$ and roughly constant in time. This makes sense since the jet seen in Fig. 4 pushes perpendicular to the initial magnetic field and effectively limits ϕ_{BH}. Because of this, the time-averaged accretion rate is the largest of the four simulations, $\sim$0.25 times the Bondi rate. The most a priori surprising case is $\psi = 60°$, which shows the largest amount of magnetic flux reaching the black hole, $\phi_{BH} \sim 60$–100, as well as the smallest accretion rate, $\dot{M} \sim 0.02$–0.1 times the Bondi rate. These curves display typical MAD behaviour similar to the $\psi = 0°$ curves. Naively, we would have expected the results for $\psi = 60°$ simulation to fall somewhere in between the $\psi = 30°$ and the $\psi = 90°$ results with a relatively small amount of magnetic flux reaching the black hole. Instead, it seems that supplying a field that is significantly tilted from vertical ultimately results in more net flux (as measured in both the absolute sense and normalized to the square root of the accretion rate, ϕ_{BH}) than a field completely aligned with the spin of the black hole. We speculate on why in Section 4.

The third panel of Fig. 8 plots the outflow efficiency, $\eta = (\dot{E} - \dot{M})/|\dot{M}|$. As expected, the simulation with the largest ϕ_{BH}
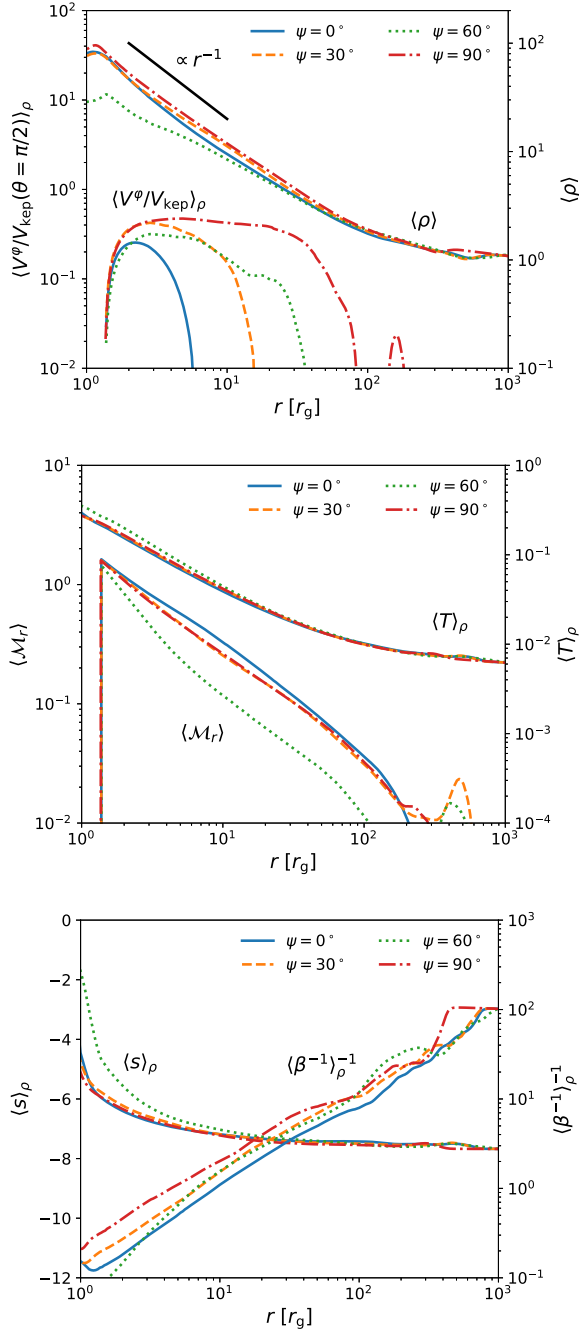
Figure 6. Angle and time-averaged fluid quantities plotted versus radius in each of our four simulations. Top: mid-plane angular velocity relative to Keplerian in the ZAMO frame, $\langle V_\varphi(\theta = \pi/2)\rangle_\rho/V_{\text{kep}}$, and mass density, $\langle\rho\rangle$. Middle: radial velocity divided by the sound speed in the ZAMO frame, $\langle\mathcal{M}_r\rangle_\rho$, and the temperature, $\langle T\rangle_\rho$. Bottom: entropy, $\langle(\gamma-1)^{-1}\log(P/\rho^\gamma)\rangle_\rho$, and plasma β, $\langle\beta^{-1}\rangle_\rho^{-1}$. Note that log here represents the natural logarithm. The accretion flow in these simulations is transonic, but the sonic radii at $\sim 2r_g$ is much closer to the event horizon than for the $a = 0$ hydrodynamic Bondi solution, where the sonic radius is $\sim 9r_g$. This is primarily due to the dynamically important, $\beta \lesssim 1$ magnetic fields located within $r \lesssim 10r_g$. Torque exerted by these fields being dragged by the rotating Kerr space–time also leads to significant ($\sim 0.5V_{\text{kep}}$) rotational velocities near the horizon $r \lesssim 10$–$30\, r_g$.

shows the largest efficiency (~ 200 per cent for $\psi = 60°$), while the simulation with the smallest ϕ_{BH} shows the smallest efficiency (either ~ 1 per cent or ~ 10 per cent for $\psi = 90°$). An efficiency of 200 per cent can only occur if energy is being extracted from the spin

of the black hole,[4] something observed in previous highly magnetized GRMHD simulations (e.g. Tchekhovskoy et al. 2011). The temporal variability of the efficiency in the $\psi = 90°$ simulation differs from the other three simulations in that there are both quiescent phases and an active phase. The active phase (with $\eta \sim 10$ per cent) occurs between $5000M \lesssim t \lesssim 15000M$, while the quiescent phases (with $\eta \sim 1$ per cent) occur for $t \lesssim 5000M$ and $t \gtrsim 15000M$. The quiescent phases correspond to the highly convective state discussed in Section 3.1 where a lack of significant vertical flux prevents the formation of a jet, instead favouring disordered reconnection-driven turbulence (see top right-hand and bottom left-hand panel of Fig. 4). The active phase arises after enough locally net vertical magnetic field is created via turbulence to form a jet.

3.3 Jet properties

In this section, we focus specifically on the magnetically dominated jet. Figs 9–12 show 2D slices at four different times of the magnetization parameter b^2/ρ zoomed out to a $200r_g \times 800r_g$ box in the x–z plane in the four simulations. At early times (i.e. 2000 M in the left-hand panel of Figs 9–12), the jets are relatively symmetric about both the spin axis of the black hole and the mid-plane. As time goes on, however, this symmetry is broken by external kink instabilities that create more complicated structures (see e.g. Bromberg & Tchekhovskoy 2016; Tchekhovskoy & Bromberg 2016; Barniol Duran, Tchekhovskoy & Giannios 2017). At some times, the jet is significantly more extended in either the upper or lower directions (e.g. the two rightmost panels of Figs 9 and 10 as well as the rightmost panel of Fig. 11) and can favour the left or right-hand side of the domain (e.g. the two rightmost panels of Fig. 9 and the three rightmost panels of Fig. 10). The latter phenomenon is particularly striking in the second panel of Fig. 10 ($\psi = 30°$), where the upper and lower jet make an approximately 90° angle with each other. While the upper jet is aligned with the direction of the initial magnetic field (inclined by 30° from the spin axis), the lower jet is perpendicular to that direction and thus the alignment in the upper jet may just be a coincidence. That conclusion is supported by the fact that the $\psi = 0°$ jet also shows a non-negligible tilt away from the spin axis in the two rightmost panels of Fig. 9 despite the field having been initially aligned with the spin axis. It is likely that the degree to which the jet is tilted is determined by stochastic symmetry breaking as it propagates through a relatively dense medium and wobbles about via kink modes.

The jets are also intermittent in the sense that there are spatial gaps between different sections (e.g. third panel of Figs 11 and 12), and their spatial extent periodically grows and diminishes. The intermittency is caused by the periodic fluctuations of the fundamental power source of the jet, the magnetic flux, seen in the top panel of Fig. 8. Without this power source, the cavities initially excised by the jet are quickly overcome by the surrounding gas as it falls inwards.

Another interesting aspect of Figs 9–12 are the bubbles that pinch off from the main body of the jet (e.g. the middle two panels of Fig. 12 and rightmost panel of Fig. 9). These are low density, magnetic pressure supported regions of tangled magnetic field that form as the jets propagate outwards through the ambient medium. They buoyantly rise through the gas until they dissipate at larger radii.

In order to further quantify the properties of the jet, we define it precisely as all regions with $b^2/2 > 1.5\rho$ (as in Liska et al. 2019b).

---

[4]For $\eta < 100$ per cent, it is also possible that the flow is extracting energy from the black hole, but it is not as easy to diagnose.
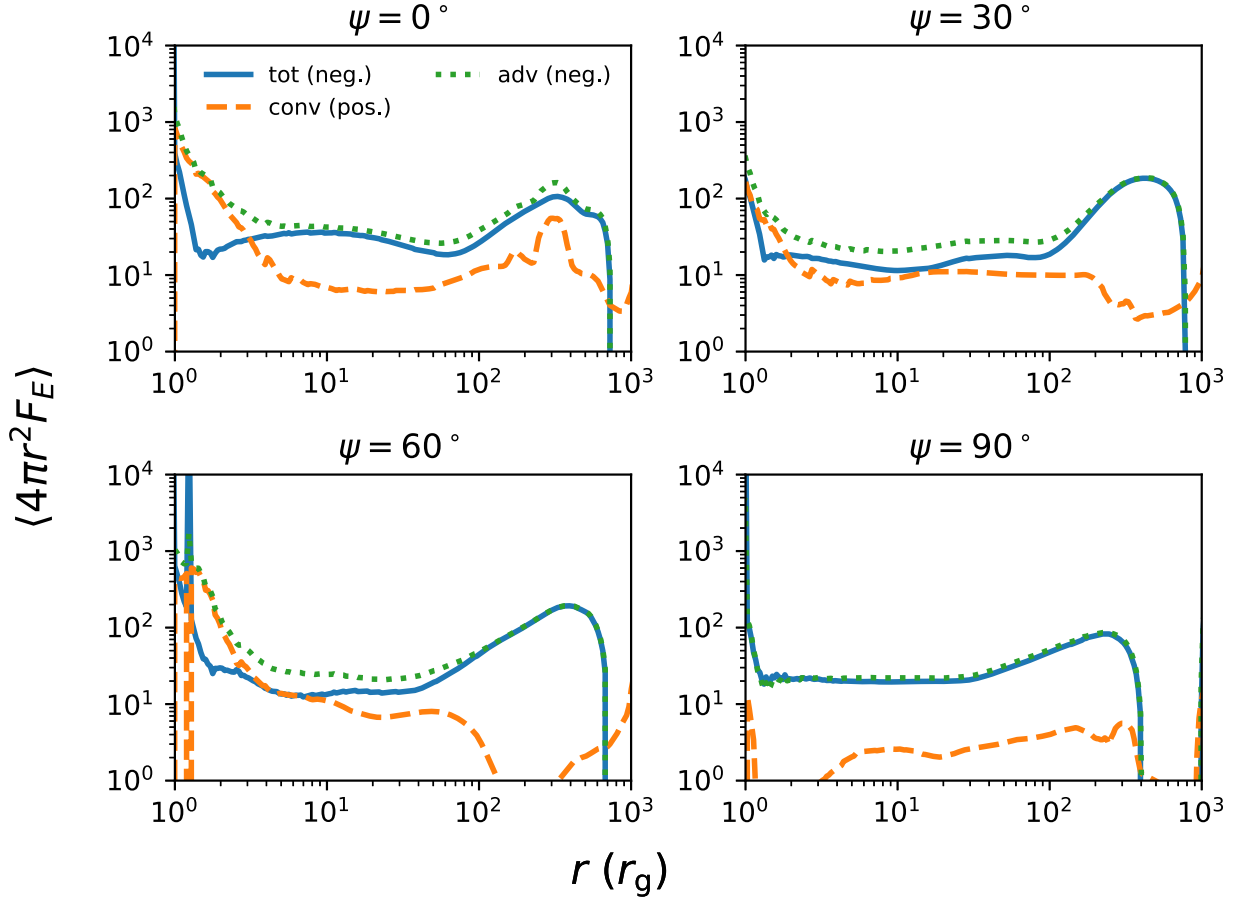
Figure 7. Flux of energy in our four different simulations, averaged over time and angle broken down into the total (solid), convective (dashed), and advective (dotted) components. Here, we restrict the averages to $|\theta - \pi/2| < \theta_H$, where θ_H is the half-angle associated with the scale height of the disc. Convection transports outwards only a fraction ($\lesssim 1/3$) of the energy being advected inwards except at the innermost radii ($r \lesssim 5$–$10\ r_g$). The convective flux is particularly small in the $\psi = 90°$ simulation, $\lesssim 0.1$ times the advective flux at all radii.

This allows us to assign radii to the upper and lower jets, $r_{\rm jet}^{+/-}$, as the maximum radii for which $b^2/2 > 1.5\rho$ and $\theta < \pi/2$ (+) or $\theta > \pi/2$ (−). Although these definitions are somewhat crude, they relatively accurately represent the behaviour seen in Figs 9–12 so they suit our purposes. $r_{\rm jet}^+$ is plotted versus time for the four simulations in the top panel of Fig. 13 (the qualitative behaviour of $r_{\rm jet}^-$ is similar). Initially, the jets expand outwards at a fraction of the speed of light but eventually stall around 300–800 r_g. At these radii, the surrounding gas is roughly uniform and stationary since the Bondi radius is $200 r_g$. After stalling, the jet radius oscillates in time, correlated directly with fluctuations in $\phi_{\rm BH}$ and η in Fig. 8. The differences between the time-averaged jet radius in the four simulations are as expected based on the differences in outflow efficiency (Fig. 8). The $\psi = 90°$ jet stalls at the smallest radius, $\sim 300 r_g$, while the $\psi = 60°$ jet stalls at the largest radius, ~ 700–$800 r_g$. The $\psi = 0°$ and $\psi = 30°$ jets stall somewhere in between, $\sim 400 r_g$.

We find that velocities inside the jet are only mildly relativistic, reaching maximum Lorentz factors $\gamma = u^t(-g^{tt})^{-1/2} \lesssim 2$ ($u^r/u^t \lesssim 0.6c$) at a few hundred r_g and then rapidly decelerating in radius near the edge of the jet.

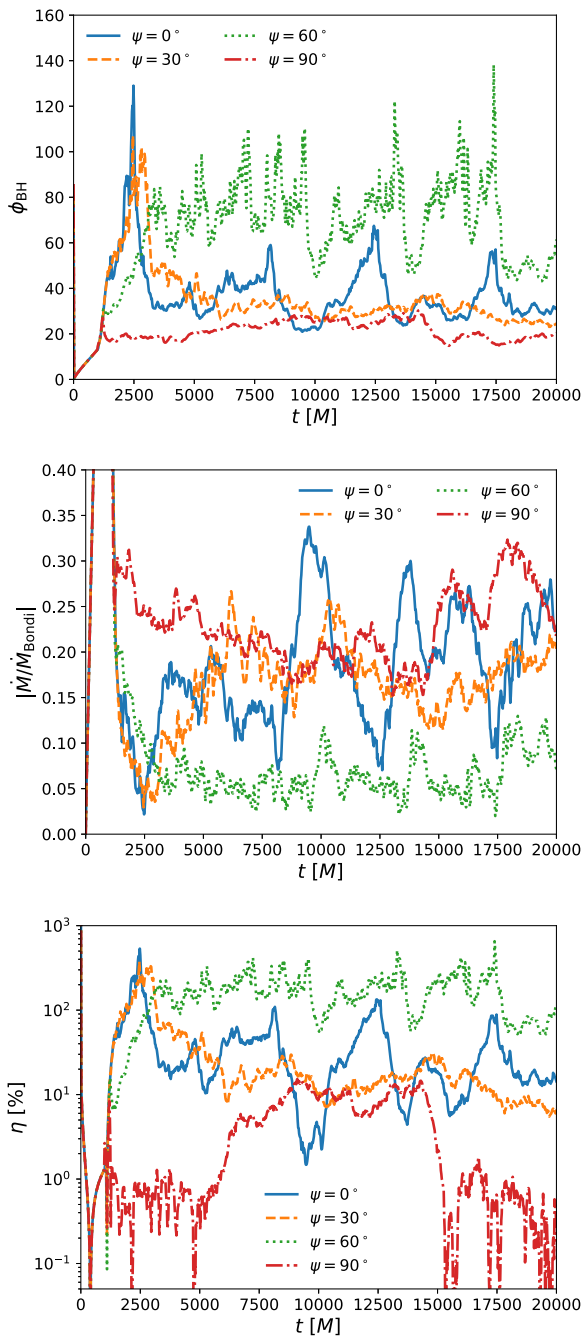We can also define a half-opening angle of the jet, $\alpha_{\rm jet}$ as the solution to the equation

$$\frac{A_{\rm jet}(r)}{2\pi} - \int_0^{\alpha_{\rm jet}} \sqrt{-g}\,d\theta = 0, \qquad (11)$$

where $A_{\rm jet}(r) \equiv 1/2 \iint H(b^2/2 - 1.5\rho)\sqrt{-g}\,d\theta\,d\varphi$ is the effective cross-sectional area of one jet (hence the factor of 1/2) and H is the Heaviside step function. The time-averaged $\alpha_{\rm jet}$ is plotted versus radius in the bottom panel of Fig. 13 for our simulations. Near the event horizon, the jets are quite wide, $\alpha_{\rm jet} \sim 30$–$40°$ as shown previously in Figs 1–4. As material in the jet flows outwards, it becomes confined to a narrower and narrower angle, decreasing in a way that is consistent with a parabolic jet profile ($A_{\rm jet} \propto r$). For example, at $r = 10 r_g$ $\alpha_{\rm jet} \sim 10$–$20°$, while at $r = 100 r_g$ $\alpha_{\rm jet} \sim$ a few degrees.

Fig. 14 shows space–time diagrams of the location of the jets (at $r = 200 r_g$) projected on to the x–y plane. More precisely, we define

$$x_{\rm jet}^+ = \frac{\iint x H(b^2/2 - 1.5\rho) H(\theta < \pi/2)\sqrt{-g}\,d\theta\,d\varphi}{\iint H(b^2/2 - 1.5\rho) H(\theta < \pi/2)\sqrt{-g}\,d\theta\,d\varphi} \qquad (12)$$

and similarly for $y_{\rm jet}^+$. The jets wobble around with time in spiral patterns characteristic of the external kink instability, which is known to occur when a highly magnetized jet attempts to penetrate a dense medium (e.g. Bromberg & Tchekhovskoy 2016; Tchekhovskoy & Bromberg 2016; Barniol Duran et al. 2017) and is generally caused by toroidally dominant fields in collimated jets (Begelman 1998; Lyubarskii 1999). As the jets in our simulations push against the surrounding gas, they decelerate, converting some of their poloidal

magnetic field to toroidal field like a spring being compressed, leading to the unstable configuration near the radial edge of the jet. As a result, its electromagnetic energy is largely converted into internal and kinetic energy by heating up and accelerating the surrounding gas. Fig. 15 demonstrates this for the $\psi = 60°$ simulation by plotting the time-averaged $\dot{E}$ versus radius, broken up into electromagnetic, kinetic, and thermal components. The thermal component starts off as negligible but steadily increases until it overtakes the electromagnetic component at $\approx 500 r_g$ (typically ~a few 100 r_g for the other three simulations with smaller jet power). At this point, the jet has blown out a low density, high-temperature cavity of much larger spatial extent than its cross-section. This is shown in Fig. 16, which plots the time-averaged radial velocity, temperature, β, and pressure in the x–z plane for the same $\psi = 60°$ simulation on an $r \sim 1000 r_g$ scale. Compared to the surrounding medium, the cavity is a factor of ~10 times hotter and ~10 times less dense so that the pressures are comparable. Most of the gas in the cavity is unbound, with velocities exceeding free-fall.

Also plotted in the top left-hand panel of Fig. 16 are velocity streamlines. Material on the edge of the jet/cavity with $\dot{r} \lesssim$ free-fall tends to circulate back towards the mid-plane and feed the inflow. In practice, while this does not significantly alter the hydrodynamic properties of the accretion flow near the Bondi radius, it can noticeably change the field geometry there (see e.g. the rightmost panel of Fig. 11 where the field lines in the $\psi = 60°$ simulation bear almost no resemblance to the initial conditions and look more like the $\psi = 0°$ simulation). Because of this effect, we are less concerned that the idealized, purely laminar magnetic fields lines in the initial conditions are artificially reducing turbulence in the mid-plane.

4 THE $\psi = 60°$ OUTLIER

Naively, one would assume that the amount of magnetic flux threading the black hole (and thus jet power) would either decrease with increasing ψ (for $0° \leq \psi \leq 90°$) because of the decreased supply of initial vertical magnetic field or be relatively independent of ψ because ϕ_{BH} would tend to saturate at some unique value determined by the balance between the outwards Lorentz force and inflow. Instead, we find that the $\psi = 60°$ simulation has the highest value of ϕ_{BH}. To determine whether this result is robust or simply caused by stochastic variation between the four simulations, we run an additional six simulations with $\psi = 15°, 45°, 52.5°, 60°, 67.5°$, and $75°$ with exactly half the resolution in each direction as the main simulations of this paper. The resulting ϕ_{BH} as function of ψ is plotted in Fig. 17 (including all 10 simulations), where ϕ_{BH} is averaged over intervals containing several limit cycles once the flux has roughly saturated.[5] With the range in ψ now finely sampled, it is clear that simulations with $40° \lesssim \psi \lesssim 80°$ have systematically higher values of ϕ_{BH} than the rest (~ 60–80 compared to ~20–40).

To understand the dependence of ϕ_{BH} on ψ shown in Fig. 17, first consider the case of a non-spinning black hole. In the limit of large Bondi radius, the initially uniform, weak magnetic field become almost entirely radial by the time it reaches the event horizon, flipping sign across a current sheet in the plane perpendicular to the initial field and containing the origin, as illustrated in Fig. 18 that plots b^2 and magnetic field lines at an early time in our simulations (at this early

Figure 8. Angle-integrated quantities plotted versus time for the four simulations. Top: Dimensionless measure of the amount of magnetic flux threading the event horizon, ϕ_{BH}. Middle: Net mass accretion rate through the horizon normalized to the Bondi rate, $|\dot{M}/\dot{M}_{Bondi}|$. Bottom: Outflow efficiency measured at $r = 5r_g$, $\eta \equiv |\dot{E} - \dot{M}|/|\dot{M}|$. The $\psi = 0°$ and $\psi = 60°$ show magnetically arrested behaviour, with flux dissipation events (i.e. rapid decreases in ϕ_{BH}) followed by large spikes in accretion rates. The other two simulations are less time variable in both magnetic flux and accretion rate, saturating at moderately smaller values of ϕ_{BH}. η is dominated by the electromagnetic energy of the jet, and reaches as high as 200–300 per cent (meaning that energy is extracted from the rotation of the black hole) for $\psi = 60°$. The other three simulations have more modest efficiencies, ~10–30 per cent on average. This is true even of the $\psi = 90°$ simulation with no net initial vertical flux, though only for $5000M \lesssim 15\,000M$ when a jet is present (see Fig. 4). At other times η is < 1 per cent.

---

[5]For most simulations, we use the interval 5000–20 000M, but for some of the lower resolution simulations the flux takes longer to saturate and so we use intervals with later start times. For example, for $\psi = 45°$ we use 16 000–25 000 M.
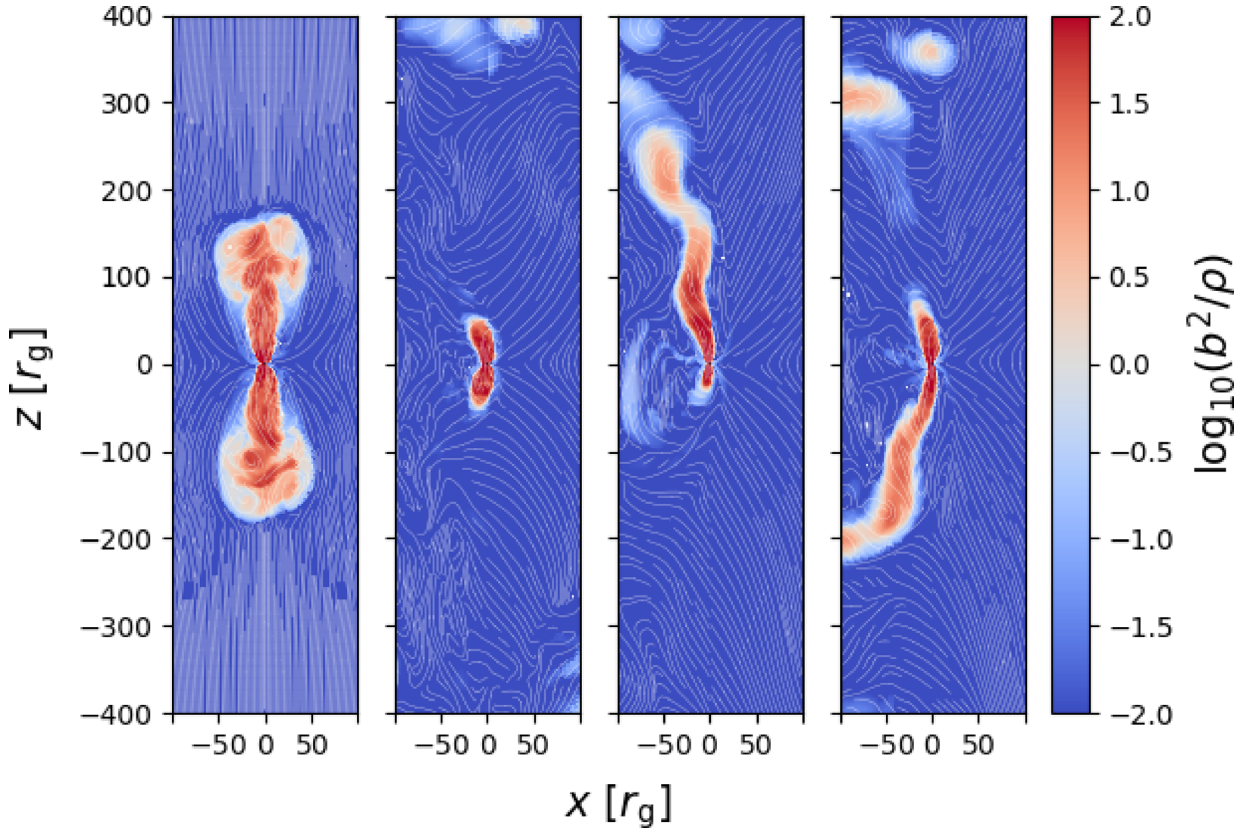
Figure 9. Azimuthal slice of the magnetization parameter b^2/ρ at four different times in our $\psi = 0°$ simulation. Starting from the top left-hand panel and proceeding to the right, the panels represent 2000, 8000, 14 000, and 20 000 M. A highly magnetized, well-collimated jet is visible at all times, though its size and orientation are significantly time-variable. It is also highly asymmetric about both the mid-plane and the polar axes, with the upper ($z > 0$) and lower ($z < 0$) portions of the jet often displaying very different behaviour. Each can be tilted by as much as 30° from the black hole spin axis at certain times.

time the effects of $a \neq 0$ are small). The field maintains this geometry all the while growing in strength until it becomes dynamically important (Bisnovatyi–Kogan & Ruzmaikin 1974). At this point, it reconnects at the location of the current sheet, which heats the gas and drives turbulence. Turbulence leads to more reconnection, and the cycle continues. Rotating the initial magnetic field simply rotates the location of the initial current sheet so that the resulting flows are essentially identical, modulo the chaotic nature of the turbulence. Now consider a rapidly spinning black hole. Once a jet is formed the inflow becomes restricted to a smaller region centred on the mid-plane (as defined by the black hole rotation axis), say, $|\theta - \pi/2| < \alpha_{\mathrm{mid}}$ that will only contain the entire angular extent of the initial current sheet if $\psi < (\pi/2 - \alpha_{\mathrm{mid}}$; assuming $\psi < 90°$). If the jet forms before the onset of turbulence then the inflow in that case would plausibly be characterized by more reconnection (and hence, more turbulence and more dissipation of the magnetic field) than the case when the initial current sheet is only partially contained in the inflow region (the rest being blown away by the jet). Less dissipation in the more laminar flows would allow for larger amount of magnetic flux to accumulate and a higher saturation value for ϕ_{BH}. This argument breaks down if the field reconnects and starts driving turbulence *before* the jet has a chance to form, which happens when ψ nearly approaches 90° since it takes longer for vertical field to accumulate via advection. Thus, there is a 'sweet spot' around $\pi/2 - \alpha_{\mathrm{mid}} < \psi < 90°$ where we would expect ϕ_{BH} to be largest. Since we find $(\pi/2 - \alpha_{\mathrm{mid}}) \gtrsim 45°$ near the horizon (bottom panel of Fig. 13), this would explain why the $\psi = 60°$ simulation has the highest value of ϕ_{BH}.

5 DEPENDENCE OF OUR RESULTS ON CERTAIN PARAMETERS

In this section, we speculate how the results of our simulations depend on certain input parameters, namely, the Bondi radius, the initial β, and the maximum magnetization, σ_{max}. Although it is beyond the scope of this work to do a comprehensive parameter survey, we can make reasonable extrapolations based on physical arguments and the results of past work in the literature. Even so, this is no substitute for systematically varying these parameters in our simulations and thus the conclusions we draw in this section should be treated as conjecture.

5.1 Dependence on Bondi radius

Our choice of $r_{\mathrm{B}} = 200r_{\mathrm{g}}$ is much less than appropriate for realistic low-luminosity AGN such as Sgr A* and M87. In practice, this limits the region of reconnection-driven turbulence in our simulations to a relatively small radial range. Since an initially uniform, weak magnetic field will grow in strength due to the compression caused by spherical inflow as $(r/r_{\mathrm{B}}^{-2}$; dominated by the radial component), the magnetic pressure will grow as $(r/r_{\mathrm{B}})^{-4}$, while the thermal pressure will grow as $\sim r^{-5/2}$ (assuming a Bondi -type flow). This means that $\beta \sim 1$ will be reached at some radius $r_{\mathrm{conv}} \approx r_{\mathrm{B}}\beta_0^{2/3}$, where the field will start reconnecting. This expression gives $r_{\mathrm{conv}} \approx 22r_{\mathrm{g}}$ for our parameters, roughly agreeing with the simulations (Fig. 6). For much larger r_{B}, r_{conv} will also be much larger and so we expect that convection will be present across several orders of magnitude in
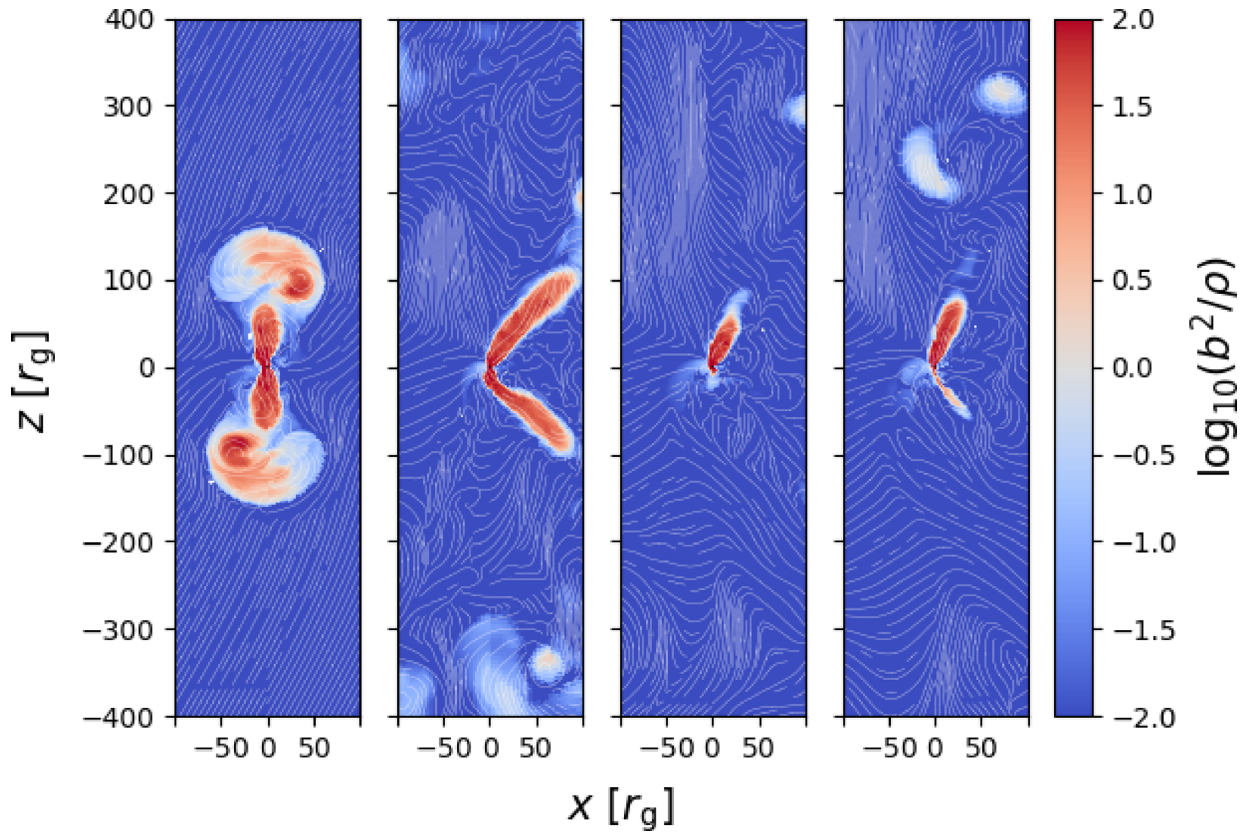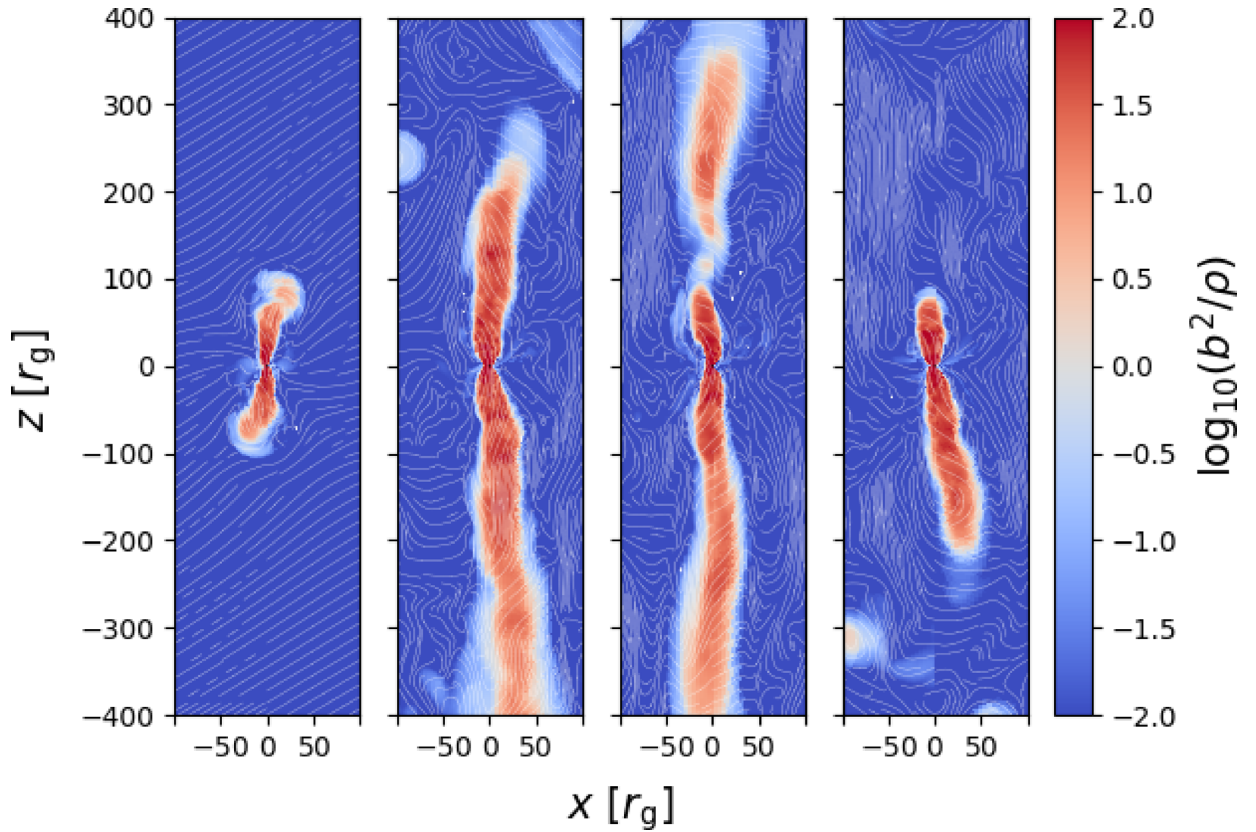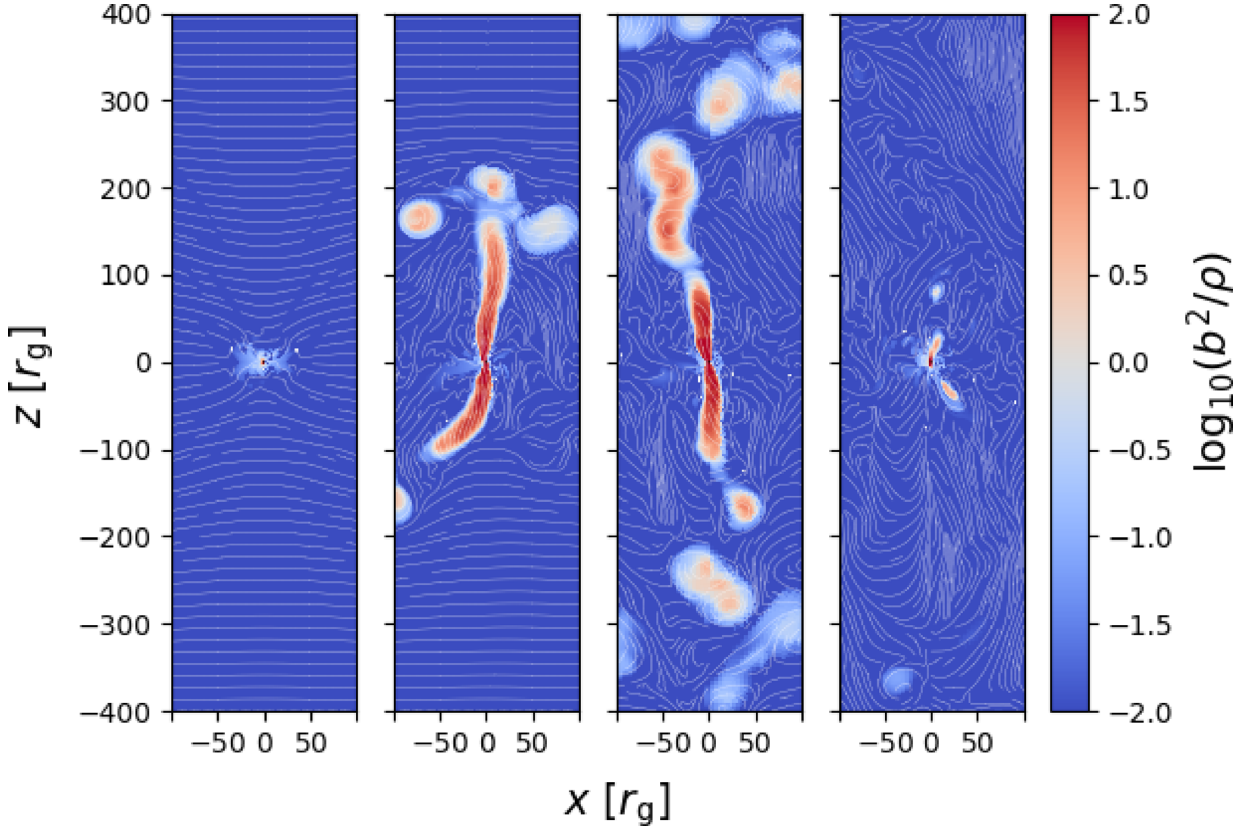
Figure 10. Same as Fig. 9 but for $\psi = 30°$.

Figure 11. Same as Fig. 9 but for $\psi = 60°$.

Figure 12. Same as Fig. 9 but for $\psi = 90°$.

radius. In this subsection, for the purposes of extrapolation we assume that the basic power-law dependences of the flow properties that we observe in these simulations where convection/turbulence occurs in a relatively narrow radial range will hold for simulations where convection/turbulence occurs in a more extended radial range. This assumption requires that a significant amount of net magnetic flux will survive transport through the larger convective regions and still reach the black hole. Because the competition between advection and diffusion of magnetic fields in such a regime is not well understood, it is not obvious how well this assumption is justified. The crux of the issue is that turbulent diffusion could, in principle, decouple the motion of the magnetic flux from the mass flux so that infall does not necessarily guarantee an accumulation of ϕ_{BH} on to the black hole.

5.1.1 ϕ_{BH} versus ψ dependence

Also uncertain is whether or not the ϕ_{BH} versus ψ dependence shown in Fig. 17 will hold for larger convective regions. Our hypothesis for why the $\psi = 60°$ simulation has the largest ϕ_{BH} (Section 4) is that a large fraction of the initial current sheet is close enough to the polar regions to be partially blown away by the jet. If the onset of convection/turbulence begins at much larger radii, this subtlety of the magnetic field geometry may be washed out by the time it reaches the event horizon even if the overall net direction is preserved. Another possibility is that the jet could stall at smaller radii than r_{conv} and have less of an influence on flux transport/reconnection. These concerns prevent us from determining whether the dependence of ϕ_{BH} on ψ seen in our models is a robust feature of spherical infall of initially coherent magnetic fields or unique to relatively small r_B. Future work varying r_B could shed more light on this issue.

5.1.2 Accretion rate

Since we expect that the radial velocity near the event horizon to always be $\propto$ free-fall $\sim c$, the $\rho \propto \rho_0(r_B/r)$ observed in our simulations implies $\dot{M} \propto \rho_0 r_B$. Since $\dot{M}_{Bondi} \propto \rho_0 r_B^{3/2}$, we predict that $\dot{M}/\dot{M}_{Bondi} \propto r_B^{-1/2}$. For Sgr A*, where $r_B \approx 2 \times 10^5 r_g$ and $\dot{M}_{Bondi} \approx 10^{-6}\,\mathrm{M}_\odot\,\mathrm{yr}^{-1}$ (Baganoff et al. 2003; Wang et al. 2013), this extrapolation would imply that $\dot{M} \sim 1.5 \times 10^{-3}$–$6 \times 10^{-3}\,\dot{M}_{Bondi} \sim 1.5$–$6 \times 10^{-9}\,\mathrm{M}_\odot\,\mathrm{yr}^{-1}$, a reasonable accretion rate given observational constraints (Marrone et al. 2006) and previous simulation-based estimates (Shcherbakov & Baganoff 2010; Mościbrodzka et al. 2014; Dexter et al. 2020a; Ressler et al. 2020b). For M87, where $r_B \approx 5 \times 10^5 r_g$ and $\dot{M}_{Bondi} \approx 0.1\,\mathrm{M}_\odot\,\mathrm{yr}^{-1}$ (Di Matteo et al. 2003), we extrapolate that $\dot{M} \sim 1 \times 10^{-3}$–$4 \times 10^{-3}\,\dot{M}_{Bondi} \sim 1$–$4 \times 10^{-4}\,\mathrm{M}_\odot\,\mathrm{yr}^{-1}$, a number in good agreement with the mean accretion rates required for GRMHD MAD models to reproduce the 230 GHz flux (Event Horizon Telescope Collaboration, 2019b) and consistent with Faraday rotation estimates (Kuo et al. 2014, though see Ricarte et al. 2020 for a discussion of why the rotation measure might not be a reliable tracer for the accretion rate).

Physically, the reason that this extrapolation predicts much smaller accretion rates than the Bondi value is not primarily due to mass outflows (though these are present near the jet boundary) but the reduced radial velocity caused by the presence of magnetic fields. The Bondi rate is appropriate for a spherically symmetric distribution of gas under the influence of gravity alone and can thus be thought of as an effective upper limit on the accretion rate for a system that includes other forces (e.g. magnetic forces), irreversible dissipation (e.g. shocks or turbulence), or non-ideal effects (e.g. conduction).
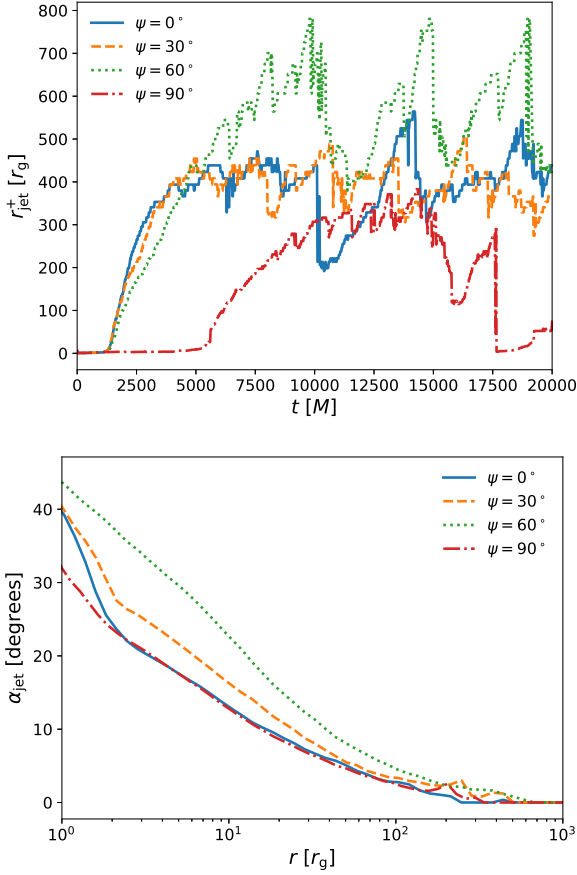
Figure 13. Upper jet radius, r_{jet}^{+}, as a function of time (top) and jet half-opening angle, α_{jet}, as a function of radius (bottom) in our four simulations. Jets initially travel outwards at a constant speed that is a fraction of the speed of light but ultimately stall at ~ 300–$700 r_{\mathrm{g}}$, at which point they periodically fall back and then re-expand. The opening angles of the jets decrease with radius in a manner consistent with a parabolic shape.

5.1.3 Jet radius

The radial extent of the jet is regulated by the kink instability, which causes the outer parts of the jet to spiral around the axis (Fig. 14) and generally become disrupted (Figs 9–12). This motion serves to dissipate the magnetic energy of the jet, heating the surrounding gas and propelling it into a wider, uncollimated outflow. The transition happens when the time-scale for kink mods to grow, t_{kink}, is sufficiently small compared to the time it takes for a fluid element to traverse the remaining height of the jet, t_{dyn}. Using an analytic model of a cylindrical, relativistic jet propagating through an external medium motivated by their simulations, Bromberg & Tchekhovskoy (2016, see also Bromberg et al. 2011) estimate that

$$\frac{t_{\mathrm{kink}}}{t_{\mathrm{dyn}}} \widetilde{\propto} \left(\frac{L_{\mathrm{jet}}}{\rho_{\mathrm{a}} r^2 \gamma_{\mathrm{jet}}^2} \right)^{1/6}, \tag{13}$$

where L_{jet} is the luminosity of the jet, $\rho_{\mathrm{a}}(r)$ is the density of the ambient medium, and γ_{jet} is the Lorentz factor of the jet. First consider $r < r_{\mathrm{B}}$, where $\rho_{\mathrm{a}} \widetilde{\propto} r_{\mathrm{B}}/r$. Assuming $L_{\mathrm{jet}} \propto \dot{E} \propto \dot{M}c^2 \propto r_{\mathrm{B}}$, equation (13) predicts that the stability properties of the jet will be independent of r_{B} in in this region (as long as γ_{jet} is roughly independent of r_{B}) and $t_{\mathrm{kink}}/t_{\mathrm{dyn}} \propto (r/r_{\mathrm{g}})^{-1/6}$. On the other hand, for $r > r_{\mathrm{B}}$, where the jets in our simulations stall, $\rho_{\mathrm{a}} \approx \rho_0$ and thus $t_{\mathrm{kink}}/t_{\mathrm{dyn}} \propto [r^2/(r_{\mathrm{B}} r_{\mathrm{g}})]^{-1/6}$.
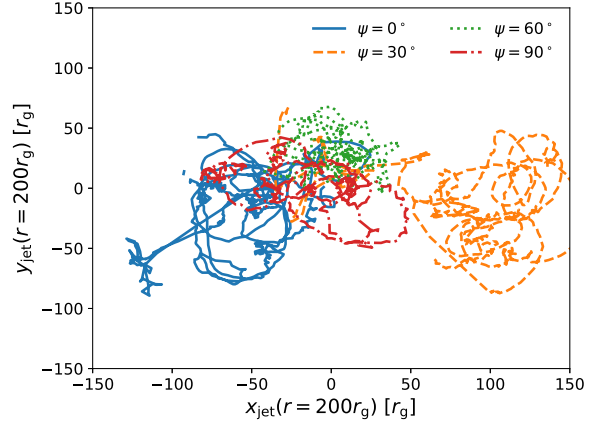
Figure 14. Space–time diagrams of the location of the jet at $r = 200 r_{\mathrm{g}}$ projected on to the x–y plane in the four simulations. The kink instability causes the jets to move around in spiral-like patterns as a function of time. With the largest jet power (Fig. 8), the $\psi = 60^{\circ}$ simulation also has smallest amplitude variations in jet location.
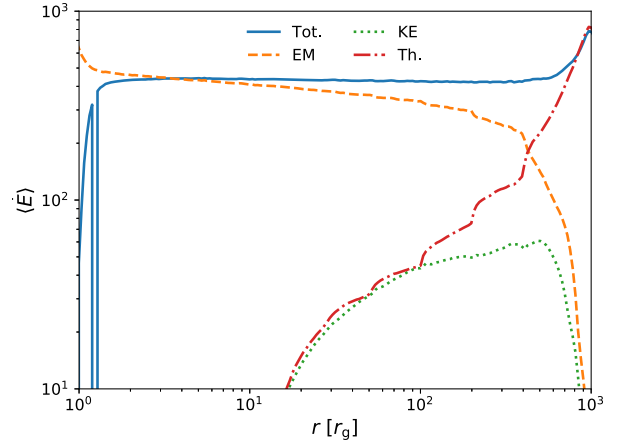
Figure 15. Radial energy flux, $\dot{E}$, broken up into total (solid), electromagnetic (dashed), kinetic (dotted), and thermal (dot–dashed) components for the $\psi = 60^{\circ}$ simulation. At small radii, the energy outflow is dominated by the Poynting-dominated jet. As the jet propagates outwards, its magnetic energy dissipates into kinetic and thermal energy. The latter dominates for $r \gtrsim 500 r_{\mathrm{g}}$. The other three simulations show qualitatively similar behaviour and are thus not shown.

In order to estimate where a jet would ultimately stall if r_{B} was $\gg 200 r_{\mathrm{g}}$, we can thus solve

$$\left. \frac{t_{\mathrm{kink}}}{t_{\mathrm{dyn}}} \right|_{\rho_{\mathrm{a}} = \rho_0 (r_{\mathrm{B}}/r)} \left(r = r_{\mathrm{jet}}, r_{\mathrm{B}} \gg 200 r_{\mathrm{g}} \right)$$

$$= \left. \frac{t_{\mathrm{kink}}}{t_{\mathrm{dyn}}} \right|_{\rho_{\mathrm{a}} = \rho_0} \left(r = 400 r_{\mathrm{g}}, r_{\mathrm{B}} = 200 r_{\mathrm{g}} \right) \tag{14}$$

for r_{jet}, where we have used $400 r_{\mathrm{g}}$ as a characteristic jet stalling radius for our simulations (Fig. 13) and approximated the density profile as a piecewise power law. Substituting equation (13) for $t_{\mathrm{kink}}/t_{\mathrm{dyn}}$ into equation (14), we find $r_{\mathrm{jet}} \approx 800 r_{\mathrm{g}}$ independent of r_{B}, which is valid as long as $r_{\mathrm{B}} \gtrsim 800 r_{\mathrm{g}}$. For $r_{\mathrm{B}} \lesssim 800 r_{\mathrm{g}}$, we replace $\rho_{\mathrm{a}} = \rho_0 (r_{\mathrm{B}}/r)$ with $\rho_{\mathrm{a}} = \rho_0$ in right-hand side of equation (14) and obtain $r_{\mathrm{jet}} \approx 400 r_{\mathrm{g}} \sqrt{r_{\mathrm{B}}/200 r_{\mathrm{g}}}$. In summary, we (roughly) predict

$$r_{\mathrm{jet}} \approx \begin{cases} 800 r_{\mathrm{g}} \sqrt{\dfrac{r_{\mathrm{B}}}{800 r_{\mathrm{g}}}} & r_{\mathrm{B}} \lesssim 800 r_{\mathrm{g}} \\ 800 r_{\mathrm{g}} & r_{\mathrm{B}} \gtrsim 800 r_{\mathrm{g}}. \end{cases} \tag{15}$$
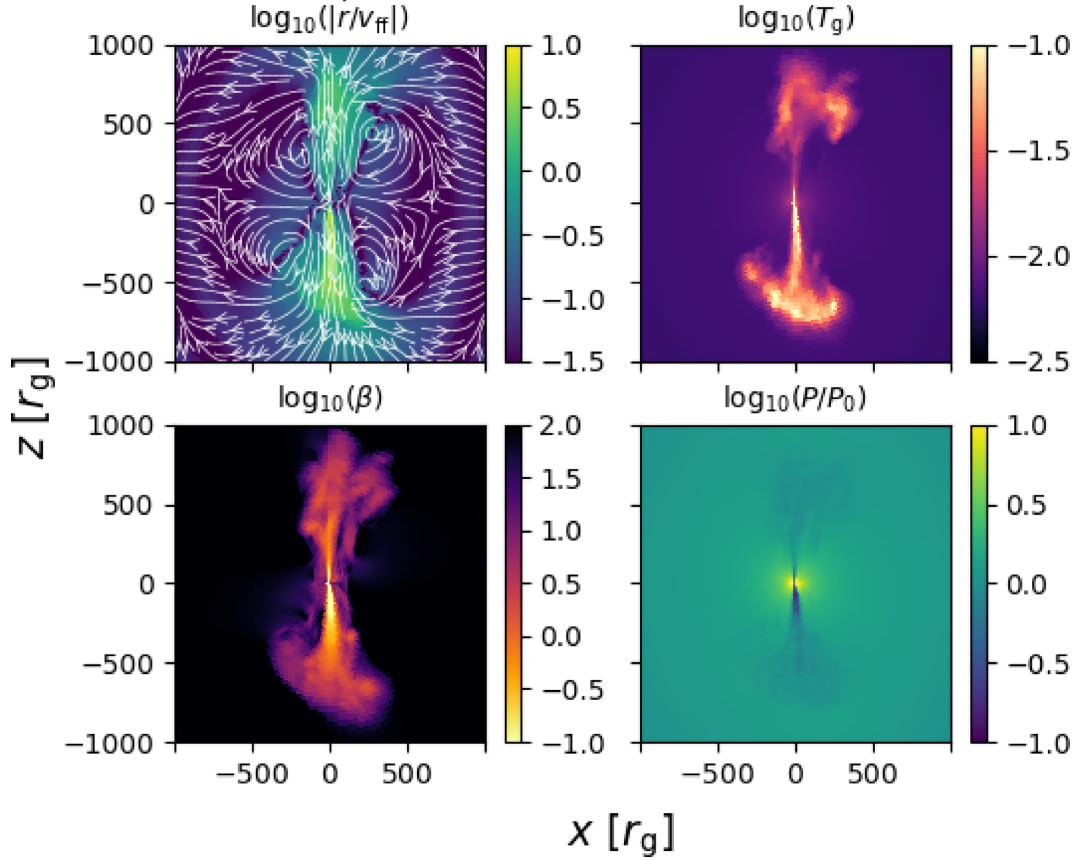
Figure 16. Time-averaged, $y = 0$ slices of four quantities in the $\psi = 60°$ simulation at large radii, where the jet breaks up due to the kink instability. Top left: magnitude of the radial velocity normalized to the free-fall speed, $|\dot{r}|/v_{\mathrm{ff}}$, overplotted with velocity streamlines. Top right: gas temperature, T_g. Bottom left: plasma β. Bottom right: pressure normalized to the initial pressure, P/P_0. The 'wobbling' of the jet (Fig. 14) caused by the kink instability carves out a cavity of hot, magnetized gas with large radial velocities. This cavity is in rough pressure equilibrium with its surroundings. Gas near the edge of the jet/cavity circulates back into the inflow, altering the supply of magnetic flux in a nonlinear way. The other three simulations show qualitatively similar behaviour and are thus not shown.
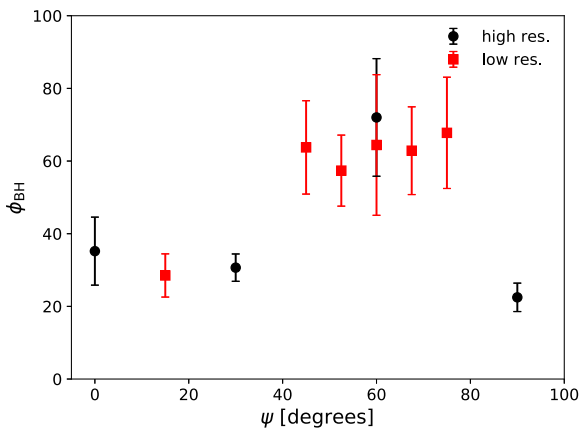
Figure 17. Dimensionless magnetic flux threading the black hole averaged over time (see main text), ϕ_{BH}, versus initial magnetic tilt angle ψ. The circles represent simulations that employ the fiducial resolution described in Section 2, the squares represent simulations that employ a resolution reduced by 2 in all three directions, while the error bars represent the standard deviation of ϕ_{BH} over the chosen time interval. There is a clear peak at $\psi \sim 40°$–$80°$ that we discuss in Section 4.

In Sgr A* and M87, $r_B \gg 800r_g$, so we expect that the jet would stall somewhere around $\sim 800\, r_g$, $\pm$ a few hundred r_g. This assumes, of course, that the linear stability criterion (equation 13) correctly predicts the scaling of the non-linear disruption of the jet by the kink instability as r_B is varied.

5.2 Dependence on initial β

All simulations that we have presented use an initial $\beta_0 = 100$. We do not expect our results to be sensitive to this value as long as it is sufficiently large ($\gtrsim 10$ or so) so that the initial magnetic field is not dynamically important. This is because no matter how small the field is at $t = 0$, the roughly spherical accretion of frozen-in field lines will lead to a configuration of nearly radial magnetic field lines near the horizon with a dependence on radius of $b^2 \propto r^{-4}$ and a magnitude that is growing with time (Bisnovatyi–Kogan & Ruzmaikin 1974). The field strength will continue to grow until it becomes dynamically important, at which point the reconnection of oppositely directed field lines heats the gas and drives turbulence (e.g. Shvartsman 1971; Meszaros 1975). In non-relativistic simulations, Pang et al. (2011) found that their results were relatively insensitive to β_0 over the range 10–1000, with the density power-law index p having only a weak dependence on this parameter, $\beta_0^{-0.098}$.
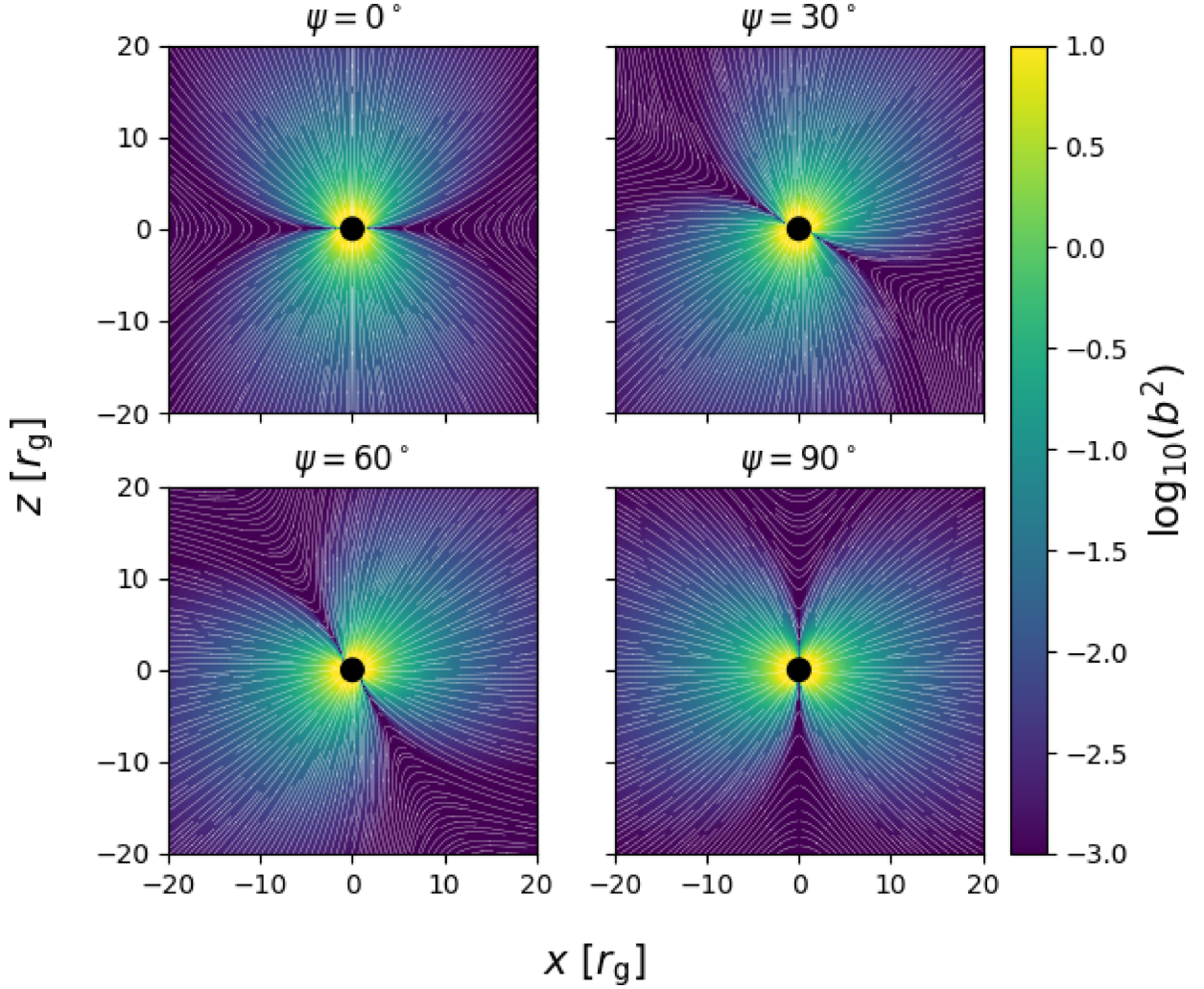
Figure 18. 2D slice in the *x*–*z* plane of b^2 overplotted with magnetic field lines at an early time ($t = 400M$) in our four simulations. Spherical advection of the magnetic field causes a current sheet of $b^2 \approx 0$ to form perpendicular to the initial magnetic field. On one side of the current sheet, field lines are mostly radial and pointed outwards, while on the other side field lines are mostly radial and pointed inwards. The current sheet itself is the location of the first reconnection events that drives turbulence. For larger tilts (i.e. $\psi = 60°$ and $\psi = 90°$), it overlaps with the polar regions that are ultimately evacuated by jets. This means that if the jet forms before the first reconnection event (as it does for $\psi = 60°$ but not $\psi = 90°$), there can be a reduced amount of turbulence and an increase in the amount of magnetic flux that reaches the event horizon.

5.3 Dependence on σ_{max}

As described in Section 2, we use a density floor to impose $\sigma \leq \sigma_{\mathrm{max}}$ = 100. While this limit presumably has little to no effect on the main body of the accretion flow (where σ is generally $\ll 1$), it effectively sets the value of σ at the base of the jets in our simulations. In reality, σ in these regions would be larger, though its precise value is unknown and may be set by pair-production processes (Blandford & Znajek 1977; Chen, Yuan & Yang 2018). A larger σ in the base of the jet (i.e. a lower mass density) would lead to a larger Lorentz factor throughout the main body of the jet, which could affect the kink stability criterion and, consequently, r_{jet}. Equation (13) predicts, however, that the dependence of $t_{\mathrm{kink}}/t_{\mathrm{dyn}}$ on γ_{jet} is relatively weak, $\propto \gamma_{\mathrm{jet}}^{-1/3}$, and the dependence on σ is probably even weaker. For example, Chatterjee et al. (2019) found that adopting value for σ_{max} of 3, 10, 50, and 100 resulted in maximum Lorentz factors of ≈ 2, 5, 8, and 10, while McKinney (2006) found that a value of $\sigma_{\mathrm{max}} = 10^4$ resulted in a maximum Lorentz factor of ≈ 10. While both of these works assumed axisymmetry (thus not able to capture kink instabilities) and empty polar regions, these assumptions would, if

anything, result in a higher conversion efficiency from magnetic to kinetic energy and a stronger dependence of γ_{jet} on σ_{max} than in our 3D, kink unstable jets that have to continually fight against the ambient medium. This is encouraging but by no means conclusive evidence that r_{jet} and the evolution of the kink instability in our simulations are not strongly sensitive to the arbitrary choice of σ_{max}.

6 COMPARISON TO PREVIOUS WORK

6.1 Non-relativistic simulations

The reconnection-driven convection present in our simulations is a feature of both convection-dominated Bondi flow (CDBF) models (Igumenshchev & Narayan 2002) and magnetically frustrated models (Pen et al. 2003; Pang et al. 2011). The fundamental difference between these two classes of solutions is the amount of energy transported by convection, F_{conv}. In CDBF models, F_{conv} is large and positive, dominating the total energy transport budget and thus requiring $\rho \propto r^{-1/2}$ in steady state. In the magnetically frustrated

model, on the other hand, the magnitude of F_{conv} is relatively small and can even be negative (that is, carrying energy inwards). This allows for the power-law index, p, of the radial density profile to be anywhere between $-3/2$ and $-1/2$ and relatively unconstrained otherwise (see Gruzinov 2001, 2013 for discussions). In essence, F_{conv} is suppressed because the magnetic field damps the convective motions, 'frustrating' its ability to transport energy. In a survey over initial magnetic field strength and Bondi radius, Pang et al. (2011) found $p \approx -1$ for low angular momentum flows of this type.

The convective flux in our simulations is weak and directed outwards (Fig. 7), consistent with the the fact that we find a $p \approx -1$ density profile that is steeper than the CDBF $p = -1/2$. At certain times (e.g. top right-hand and bottom left-hand panel of Fig. 4), the density and magnetic field distribution in our $\psi = 90°$ simulation looks quite similar to those in the Pen et al. (2003, their fig. 1) and Pang et al. (2011, their fig. 1) simulations, with turbulent motions creating fairly random structure with no preferred direction. At other times in the same simulation (e.g. bottom right-hand panel of Fig. 4) and at all times (after the initial transient period) in the other simulations, however, the jets powered by the spinning black hole evacuate the polar regions of matter and localize the turbulence to the mid-plane. These black hole spin-powered jets have no analogue in non-relativistic MHD.

While we do see a reduced inwards radial velocity compared to the hydrodynamic case (as evidenced by the critical sonic point moving inwards from $\sim 8.8 \, r_{\mathrm{g}}$ to $\sim 2 \, r_{\mathrm{g}}$ (Fig. 6), we do not find the $\sim$zero radial velocities characteristic of the nearly hydrostatic CDBF and magnetically frustrated solutions. This is a strictly GR effect, as all flows must pass through a sonic point before reaching the event horizon. The stronger outwards force provided by a combination of magnetic fields and pressure can only delay the inevitable by moving the sonic point towards smaller radii. If we were to extend our simulations to larger r_{B}, the convective/turbulent zone would also extend to larger radii and could plausibly reach a nearly hydrostatic state in the region where GR effects are negligible.

6.2 GRMHD torus/jet simulations

Two of our simulations ($\psi = 0°$ and $\psi = 60°$) appear to be magnetically arrested based on the traditional build-up and dissipation cycle seen in ϕ_{BH} and the associated fluctuations in accretion rate caused by the brief repulsion of matter from near the black hole. The other two simulations ($\psi = 30°$ and $\psi = 90°$) do not appear to be fully arrested since ϕ_{BH} and $\dot{M}$ are much more stable with time, yet they are likely just under the threshold in magnetic flux to reach the arrested state. Given that conclusion, it is instructive to compare our results to previous GRMHD MAD simulations (e.g. Igumenshchev et al. 2003; Tchekhovskoy et al. 2011; Narayan et al. 2012; Chael et al. 2019; White et al. 2019a). To first approximation, Figs 1–4, which show 2D slices of mass density and magnetic field lines, look remarkably similar to GRMHD MAD simulations at most times. Both have evacuated, strongly magnetized polar regions with a large amount of coherent/vertical magnetic field lines. Both see accretion via thin, non-axisymmetric streams due to the magnetic field strongly compressing the inflow close to the horizon (e.g. Igumenshchev et al. 2003 ; see also, our Fig. 5 that shows mid-plane slices of β for $\psi = 30°$). These similarities between torus-based MADs and our initially ZAMO simulations are, perhaps, not that surprising because MAD flows are generally more sub-Keplerian than SANE flows (e.g. Narayan et al. 2012) and the magnetic fields dragged by the $a = 0.9375$ black hole in our models provide enough torque on the gas

to result in rotation rates that are a significant fraction of Keplerian near the horizon (top panel of Fig. 6).

Jets in torus simulations without any other ambient medium are generally able to freely expand radially since the polar regions are essentially vacuum. This allows for them to reach much larger distances and Lorentz factors than we see in our simulations (e.g. McKinney 2006; Chatterjee et al. 2019). In this respect, our simulations are more similar to those performed by Bromberg & Tchekhovskoy (2016), Tchekhovskoy & Bromberg (2016), and Barniol Duran et al. (2017), where the jets were embedded in spherical interstellar mediums of various density profiles ρ^{-s}. Bromberg & Tchekhovskoy (2016) provided an analytical model for the jet as a function of height and found that for $s < 2$ it becomes more unstable to the external kink instability at larger distances from the black hole, predicting that this would lead to the jet stalling or even breaking up. Consistent with that expectation, the jets in our simulations (which show $s \approx 1$ for $r \lesssim r_{\mathrm{Bondi}}$ and $s \approx 0$ for $r \gtrsim r_{\mathrm{Bondi}}$) do both of those things (Figs 13 and 9–12). Note that the value of s in this work for $r \lesssim r_{\mathrm{B}}$ is not a parameter but is determined by the dynamics of the accretion flow.

Simulations of tilted discs find that the jets at large radii tend to align perpendicular to the large-scale disc (e.g. White et al. 2019b; Liska et al. 2020a). This is primarily caused by the jet propagating through the pre-evacuated, low-density funnel carved out by the initial torus. This region is the path of least resistance for the Poynting flux to travel outwards (as opposed to penetrating through the outer disc). Since our simulations start with a ZAMO, spherical distribution of gas, the jets have no other option but to penetrate through the ambient medium. This prevents them from getting systematically channelled away from the black hole spin axis.

6.3 Wind-fed accretion on to Sgr A*

We now compare our results to the simulations that inspired them in the first place, namely, the GRMHD wind-fed Sgr A* accretion simulations of Ressler et al. (2020b), hereafter R20. Both sets of simulations display magnetically confined mid-planes, evacuated polar regions, magnetically arrested behaviour, and relatively low β, coherent magnetic fields. Both also find $\rho \tilde{\propto} r^{-1}$, though it is not clear that it is for the same reasons. In Ressler et al. (2020b), the density profile was caused by the underlying distribution of angular momentum with accretion rate in material being fed from large radii, while here it is a result of 'magnetically frustrated' convection in a pressure supported configuration. Why exactly the latter results in an r^{-1} density profile is an open question. Gruzinov (2013) argued that if there was some physical process enforcing a constant momentum flux (i.e. $\dot{P} \propto \rho v_r^2 r^2 = $ const. in the non-relativistic regime) then $\rho \propto r^{-1}$ follows as a natural consequence. $\dot{P} = $ const. can be achieved in a steady state only if gravity, pressure, and magnetic forces are perfectly balanced. While this does seem to be the case in the non-relativistic simulations (e.g. fig. 2 in Pen et al. 2003), in our simulations $\dot{P}$ increases with decreasing radius. The true reason for the r^{-1} density scaling may just be the less satisfying observation that the simulations fall somewhere between Bondi-type flows and convection-dominated accretion flow type flows, so the density power-law index must fall somewhere in between $-3/2$ and $-1/2$. It is also not clear if our simulations have sufficiently large dynamic range in radius to determine the truly self-similar scaling of the density profile.

The most obvious difference between the accretion flow in this work and that found in R20 is the nature of the polar regions. Since R20 used $a = 0$, the poles were evacuated due to a high concentration of vertical magnetic fields but lacked the toroidal field

strength necessary to drive powerful jets. As a result, the flow became quasi-spherical past a few 10s of r_g. Furthermore, these magnetic poles changed direction with time (corresponding to variations in the net field being fed from larger radii), also tilting the gas away from the previous mid-plane. As we have shown, because the black hole in our simulations is rapidly spinning, it strongly winds up the poloidal magnetic field in the toroidal direction, producing jets that reach to ∼hundreds of r_g. While the jets at large radii can be significantly tilted with respect to the black hole spin due to propagation effects and the kink instability, near the horizon the they are always aligned with the spin axis regardless of initial magnetic field orientation. We expect that if the R20 simulations were run with a large black hole spin, they would undoubtedly feature a jet that would disrupt the nature of the flow out to a relatively large radius and would most likely be less prone to oscillations in the location of the mid-plane.

6.4 Spherical infall around post-merger black hole

As this work was in the latter stages of preparation, Kelly et al. (2020, hereafter K20) appeared on arXiv presenting the results of a parallel study of low angular momentum GRMHD accretion on to rotating black holes in the context of black hole merger remnants, focusing mainly on the orientation and power of the resulting jet. The initial conditions used in their simulations were essentially the same as those used here: uniform pressure, density, and magnetic field of varying inclination angles with respect to the black hole spin. The main differences were that they (1) assumed a black hole spin of $a = 0.69$, lower than our $a = 0.9375$; (2) smaller Bondi radii (higher initial gas temperatures), $r_B \approx 8$–$81\, r_g$ compared to our $r_B = 200\, r_g$; and (3) an adiabatic index appropriate for radiation pressure-supported gas, $\gamma = 4/3$. Their fiducial model had $r_B \approx 13\, r_g$.

In contrast to our results, K20 found that the jets in their simulations only aligned with the spin axis of the black hole for $r \lesssim 30\, r_g$, while at larger radii the jets aligned with the initial magnetic field direction. Moreover, they found jet power to monotonically decrease with ψ and found no evidence of the $\psi \sim 40$–$80°$ peak in η as we do (see bottom panel of Figs 8, 17, and Section 4) seen in our simulations. We believe that this is predominantly because the K20 simulations are in an entirely different parameter regime than ours, where the dynamical range in radius is very small and any extrapolation in Bondi radius breaks down. This can be seen from their plots of various quantities versus 'κ', their proxy for the entropy/temperature of the initial gas which relates directly to r_B. For $r_B \lesssim 13\, r_g$, their simulations are roughly independent of r_B, while for $r_B \gtrsim 13\, r_g$ they show an increase of $|\dot{M}|$, $\dot{E}$, and η with increasing r_B. Moreover the simulations with smaller r_B are much less variable in time than those with larger r_B. Thus, there is a clear transition at $r_B \sim 13\, r_g$; the regime of $r_B \lesssim 13\, r_g$ is appropriate for some merger scenarios (and perhaps other stellar-mass-sized black holes), while the regime of $r_B \gtrsim 13\, r_g$ is appropriate for active galactic nuclei. Since K20 focused on the former while we focus on the latter, our works are complementary.

7 CONCLUSIONS

We have presented GRMHD simulations of spherical accretion on to a rotating black hole modified by the presence of uniform, relatively weak magnetic fields of various tilt angles with respect to the black hole spin. As the field is advected inwards, it forms current sheets and reconnects, dissipating magnetic energy and driving turbulence

(Figs 1–4). Similar to previous non-relativistic 'magnetically frustrated' models, we find that convection does not efficiently transport energy outwards (Fig. 7) and the mass density scales as $\bar{\alpha}\, r^{-1}$ (Fig. 6). Our simulations are either magnetically arrested or very close to magnetically arrested, with the dimensionless magnetic flux, ϕ_{BH} saturating at 20–80, often showing limit cycles of slow build-up followed by rapid dissipation (Fig. 8). Torque caused by frame dragging of magnetic field lines threading the rapidly spinning black hole is enough to result in significant (up to ∼0.5 Keplerian) angular velocities near the event horizon (Fig. 6) that may be enough to cause Doppler asymmetry in the 230 GHz images (e.g. as in EHT observations of M87, Event Horizon Telescope Collaboration 2019a).

All of our simulations form strongly magnetized jets that predominantly align with the spin axis of the black hole. While there are times when the jets can be significantly tilted, this tilt does not seem to correlate with ψ (the initial magnetic field direction), but rather results from symmetry breaking as the turbulently fed jet plows through the surrounding gas (Figs 9–12). At larger radii, the jet dynamics become dominated by the kink instability (Fig. 14), ultimately becoming disrupted at a few hundred r_g (Fig. 13) at which point they transition into an uncollimated outflow of hot gas reaching to ∼1000 r_g (Fig. 16). The dissipation mechanism of the kink modes is likely magnetic reconnection near the jet wall boundary (Bromberg et al. 2019), which could in turn accelerate particles to high energy (Davelaar et al. 2020) and contribute to non-thermal emission.

The nature of our simulations is highly stochastic. Not only are the dynamics of the accretion flow governed by reconnection-driven turbulence, the dynamics and shape of the jet are governed by the kink instability and interaction with the turbulent ambient medium. This is evident by the various contours of density, β, and b^2/ρ plotted in Figs 1–4, 5, and 9–12 that vary dramatically as a function of time and frequently display large global asymmetries. Small changes in the initial conditions such as the tilt of the magnetic field (ψ) could therefore lead to completely different realizations of the flow, accounting for much of the variation between the simulations we have presented. All things considered, the dynamics of the flow do not depend strongly on ψ except for a couple of special cases.

The first case is $\psi = 90°$ where there is exactly zero net initial vertical flux (and presumably for ψ close to $90°$): the jet takes longer to form, is less efficient than the other simulations, and is intermittent even at horizon scales; all because vertical flux can only be generated through turbulent motions. The second case is $\psi \sim 40°$–$80°$ where there is a peak in the magnetic flux threading the horizon, ϕ_{BH}, (Fig. 17) that is a factor of $\lesssim 2$ higher than simulations with $\psi \lesssim 40°$ and $\psi \gtrsim 80°$. We suspect that this range in angles represents a 'sweet spot' where there is slightly less turbulence inhibiting the accretion of magnetic flux because the large-scale current sheet is partially blown away by the polar outflow and yet there still enough initial vertical flux to form a jet before the onset of reconnection (see Section 4).

The fact that even the $\psi = 90°$ simulation forms (at times) a relatively high efficiency jet with $\eta \lesssim 20$ per cent (third panel of Fig. 8) gives further evidence that a large-scale net vertical flux is not necessarily a prerequisite for Blandford & Znajek (1977) jet formation. This was previously shown for flows with larger angular momentum where an MRI-driven dynamo can convert toroidal magnetic field into poloidal magnetic field (Parfrey, Giannios & Beloborodov 2015; Christie et al. 2019; Liska, Tchekhovskoy & Quataert 2020b). Here, we find that turbulent motions alone can produce enough local net vertical magnetic flux to power a jet from an already mostly poloidal but zero net vertical flux field. These results suggest that jets may be ubiquitous in systems with rapidly

rotating black holes regardless of the magnetic field geometry in the accretion flow's source.

The simulations presented in this work may be a reasonable model for Sgr A*. Magnetically arrested-type flows have been favoured in several recent analyses comparing models to observations due to (1) the relatively high levels of linear polarization observed in the mm emission (models with less magnetic flux tend to require higher accretion rates that can depolarize the emission, Jiménez-Rosales & Dexter 2018; Dexter et al. 2020a) and (2) the relatively large amount of vertical magnetic field required to reproduce the near-infrared flare polarization periodicity (Gravity Collaboration 2018, 2020; Dexter et al. 2020b; Porth et al. 2020). Moreover, wind-fed GRMHD accretion simulations that take into account the Wolf-Rayet stellar winds primarily sourcing the accretion flow naturally evolve into an arrested state (Ressler et al. 2020b). On the other hand, magnetically arrested models are known to produce powerful jets (at least for rapidly spinning black holes, e.g. Tchekhovskoy et al. 2011) and yet there is no unambiguous detection of a collimated jet in Sgr A*. Our simulations suggest, however, that this fact does not necessarily rule out the arrested model. Feeding by stellar winds can result in a quasi-spherical distribution of gas outside the inner horizon-scale that pressure-confines the jet prompting dissipation through the kink instability. If this happens well inside the Bondi radius, then larger-scale observations may only be able to probe the hot, matter-dominated outflow blown out by the unstable jet 'head' as it dissipates (e.g. Fig. 16). In fact, recent work using ALMA may have detected just that, finding evidence for a high-velocity, bipolar outflow with an opening angle of $\sim 30°$ extending from $\sim 7 \times 10^5 \, r_g$ to $\sim 10^8 \, r_g$ (Royster et al. 2019; Yusef-Zadeh et al. 2020). Alternatively, Sgr A* could be slowly spinning or the jet may be pointed directly at us. Finally, the r^{-1} dependence of the mass density that we find in our simulations (Fig. 6) is consistent with observations that use different methods to probe multiple different scales of the gas surrounding Sgr A* (Xu et al. 2006; Gillessen et al. 2019).

It is less clear whether our simulations represent a viable model for M87 or other similar galactic nuclei. Resolved X-ray emission at the Bondi radius of M87 can be fit with an $\rho \propto r^{-1}$ distribution (Russell et al. 2015), as in our simulations, though it is unknown if this dependence persists to smaller radii. In order to reproduce the unambiguous, well-collimated jet observed out to $\sim 10^6$–$10^7 \, r_g$ we would require the jets in our simulations to be stable to kink instabilities out to radii $\gtrsim 10^4$ times what we see here (Fig. 13). Simply increasing the Bondi radius to a more realistic value may accomplish this, but based on an (admittedly uncertain) extrapolation we have argued that the radius at which the jet disrupts may be independent of Bondi radius (see Section 5.1.1 and the next paragraph for a discussion). This could indicate that M87 is fed in a different manner than the Galactic Centre, with less low angular momentum gas and more disc-like accretion. Indeed, even if the M87 black hole is predominantly fed by stellar winds (which is not clear given the larger hot gas reservoir in the inner intracluster medium of Virgo), the nature of this feeding *must* be different in some respects since the much larger (absolute) accretion rate requires a much larger number of winds to sustain. This is especially true given that in Sgr A* only a handful of winds end up contributing to the accretion rate (Loeb 2004; Cuadra et al. 2008; Ressler et al. 2018).

The self-consistent formation of the rising, buoyant bubbles (or cavities) in our simulations due to a combination of the kink instability and time variability of the jet (Figs 9–12) may be broadly analogous to what occurs in galaxy clusters (e.g. Fabian et al. 2000; Blanton et al. 2010), though the spatial and temporal scales we simulate are orders of magnitude smaller than those observed in clusters. If the estimated scalings of our results with r_B (Section 5.1.1) are correct, then even for much larger r_B these cavities would never reach the sizes and distances required to match observations. On the other hand, if the flow had more angular momentum so that the poles were pre-evacuated, the jet could potentially reach the required distances before becoming kink unstable enough to produce bubbles.

For computational reasons, we have focused on one particular Bondi radius ($r_B = 200 r_G$) that is orders of magnitude less than the actual Bondi radii for real systems, including both M87 and Sgr A*. Using the dependence on radius of ρ and the kink stability criteria, we extrapolated to larger $r_B \gg 200 r_g$ (Section 5.1.1) to predict that $\dot{M}/\dot{M}_{Bondi} \propto r_B^{-1/2}$ and $r_{jet} \propto$ const, where r_{jet} is the radius at which the jet disrupts by the kink instability. However, since we have not rigorously tested these dependencies by running additional simulations with larger r_B, they should be taken with a grain of salt. Future work can test these predictions using a parameter survey in r_B or by using the actual Bondi radius in a multiscale, multiple simulation technique to extend the dynamic range in the manner of R20.

We have also focused on one particular value of σ_{max}, the maximum $\sigma \equiv b^2/\rho$ allowed in the simulations, as well as one particular value of the initial β. It is unclear the degree to which our results are affected by these choices. In Sections 5.2 and 5.3, we argue that the dependence should be relatively weak based on previous simulations in the literature, though none of those works had an entirely similar set-up as we have here. For β, the hope is that for any initial $\beta \gg 1$, the inward advection of magnetic field would ultimately lead to approximately the same steady state with larger β just taking longer to reach that state. For σ_{max}, realistic astrophysical jets likely have σ_{max} orders of magnitude larger than the $\sigma_{max} = 100$ imposed here, which if the conversion of magnetic to kinetic energy in the jets was 100 per cent efficient, this would lead to orders of magnitude larger Lorentz factors. This is an important consideration since jets with larger Lorentz factors could be even more unstable to kink modes (equation 13). However, GRMHD jets tend to be rather inefficient at converting magnetic to kinetic energy even in 2D where they are kink stable, which makes γ_{jet} not as strongly dependent on σ_{max}. We expect this to be even more true in the 3D, kink unstable jets we have presented here and thus we can reasonably hope that the main conclusions drawn in this work are not strongly sensitive to σ_{max}.

DATA AVAILABILITY

The data underlying this paper will be shared on reasonable request to the corresponding author.

REFERENCES

Baganoff F. K. et al., 2003, ApJ, 591, 891
Balbus S. A., Hawley J. F., 1991, ApJ, 376, 214
Ball D., Özel F., Psaltis D., Chan C.-K., 2016, ApJ, 826, 77
Barniol Duran R., Tchekhovskoy A., Giannios D., 2017, MNRAS, 469, 4957
Begelman M. C., 1998, ApJ, 493, 291
Bicak J., Janis V., 1985, MNRAS, 212, 899
Bisnovatyi–Kogan G. S., Ruzmaikin A. A., 1974, Ap&SS, 28, 45
Blandford R. D., Znajek R. L., 1977, MNRAS, 179, 433
Blanton E. L., Clarke T. E., Sarazin C. L., Randall S. W., McNamara B. R., 2010, Proc. Natl Acad. Sci., 107, 7174
Boyer R. H., Lindquist R. W., 1967, J. Math. Phys., 8, 265
Bromberg O., Tchekhovskoy A., 2016, MNRAS, 456, 1739
Bromberg O., Nakar E., Piran T., Sari R., 2011, ApJ, 740, 100
Bromberg O., Singh C. B., Davelaar J., Philippov A. A., 2019, ApJ, 884, 39
Calderón D., Cuadra J., Schartmann M., Burkert A., Russell C. M. P., 2020, ApJ, 888, L2
Chael A. A., Narayan R., Sądowski A., 2017, MNRAS, 470, 2367
Chael A., Rowan M., Narayan R., Johnson M., Sironi L., 2018, MNRAS, 478, 5209
Chael A., Narayan R., Johnson M. D., 2019, MNRAS, 486, 2873
Chandra M., Foucart F., Gammie C. F., 2017, ApJ, 837, 92
Chan C.-K., Psaltis D., Özel F., Narayan R., Sądowski A., 2015, ApJ, 799, 1
Chatterjee K., Liska M., Tchekhovskoy A., Markoff S. B., 2019, MNRAS, 490, 2200
Chatterjee K. et al., 2020, MNRAS, 499, 362
Chen A. Y., Yuan Y., Yang H., 2018, ApJ, 863, L31
Christie I. M., Lalakos A., Tchekhovskoy A., Fernández R., Foucart F., Quataert E., Kasen D., 2019, MNRAS, 490, 4811
Cuadra J., Nayakshin S., Springel V., Di Matteo T., 2005, MNRAS, 360, L55
Cuadra J., Nayakshin S., Springel V., Di Matteo T., 2006, MNRAS, 366, 358
Cuadra J., Nayakshin S., Martins F., 2008, MNRAS, 383, 458
Davelaar J., Philippov A. A., Bromberg O., Singh C. B., 2020, ApJ, 896, L31
De Villiers J.-P., Hawley J. F., 2003, ApJ, 589, 458
Dexter J. et al., 2020a, MNRAS, 494, 4168
Dexter J. et al., 2020b, MNRAS, 497, 4999
Di Matteo T., Allen S. W., Fabian A. C., Wilson A. S., Young A. J., 2003, ApJ, 582, 133
Event Horizon Telescope Collaboration, 2019a, ApJ, 875, L1
Event Horizon Telescope Collaboration, 2019b, ApJ, 875, L5
Fabian A. C. et al., 2000, MNRAS, 318, L65
Fishbone L. G., Moncrief V., 1976, ApJ, 207, 962
Foucart F., Chandra M., Gammie C. F., Quataert E., Tchekhovskoy A., 2017, MNRAS, 470, 2240
Fragile P. C., Blaes O. M., Anninos P., Salmonson J. D., 2007, ApJ, 668, 417
Gammie C. F., McKinney J. C., Tóth G., 2003, ApJ, 589, 444
Gillessen S. et al., 2019, ApJ, 871, 126
Gravity Collaboration, 2018, A&A, 618, L10
Gravity Collaboration, 2020, A&A , 643, A56
Gruzinov A., 2001, ApJL, preprint (arXiv:astro-ph/0104113)
Gruzinov A., 2013, preprint (arXiv:1311.5813)
Hawley J. F., Smarr L. L., Wilson J. R., 1984, ApJ, 277, 296
Igumenshchev I. V., Narayan R., 2002, ApJ, 566, 137
Igumenshchev I. V., Narayan R., Abramowicz M. A., 2003, ApJ, 592, 1042
Jiménez-Rosales A., Dexter J., 2018, MNRAS, 478, 1875
Johnson B. M., Quataert E., 2007, ApJ, 660, 1273
Kelly B. J., Eteinne Z. B., Golomb J., Schnittman J. D., Baker J. G., Noble S. C., Ryan G., 2020, Phys. Rev. D, preprint (arXiv:2010.11259)
Kerr R. P., 1963, Phys. Rev. Lett., 11, 237
Kuo C. Y. et al., 2014, ApJ, 783, L33
Liska M., Hesp C., Tchekhovskoy A., Ingram A., van der Klis M., Markoff S., 2018, MNRAS, 474, L81
Liska M. et al., 2019a, MNRAS, preprint (arXiv:1912.10192)
Liska M., Tchekhovskoy A., Ingram A., van der Klis M., 2019b, MNRAS, 487, 550
Liska M., Hesp C., Tchekhovskoy A., Ingram A., van der Klis M., Markoff S. B., Van Moer M., 2020a, MNRAS, in press

Liska M., Tchekhovskoy A., Quataert E., 2020b, MNRAS, 494, 3656
Loeb A., 2004, MNRAS, 350, 725
Lyubarskii Y. E., 1999, MNRAS, 308, 1006
Mao S. A., Dexter J., Quataert E., 2017, MNRAS, 466, 4307
Marrone D. P., Moran J. M., Zhao J.-H., Rao R., 2006, ApJ, 640, 308
McKinney J. C., 2006, MNRAS, 368, 1561
Meszaros P., 1975, A&A, 44, 59
Michel F. C., 1972, Astrophys. Space Sci., 15, 153
Mościbrodzka M., Gammie C. F., Dolence J. C., Shiokawa H., Leung P. K., 2009, ApJ, 706, 497
Mościbrodzka M., Falcke H., Shiokawa H., Gammie C. F., 2014, A&A, 570, A7
Mościbrodzka M., Falcke H., Shiokawa H., 2016, A&A, 586, A38
Narayan R., Yi I., 1995, ApJ, 444, 231
Narayan R., Igumenshchev I. V., Abramowicz M. A., 2000, ApJ, 539, 798
Narayan R., Igumenshchev I. V., Abramowicz M. A., 2003, PASJ, 55, L69
Narayan R., Sądowski A., Penna R. F., Kulkarni A. K., 2012, MNRAS, 426, 3241
Özel F., Psaltis D., Narayan R., 2000, ApJ, 541, 234
Pang B., Pen U.-L., Matzner C. D., Green S. R., Liebendörfer M., 2011, MNRAS, 415, 1228
Parfrey K., Giannios D., Beloborodov A. M., 2015, MNRAS, 446, L61
Pen U.-L., Matzner C. D., Wong S., 2003, ApJ, 596, L207
Penna R. F., Kulkarni A., Narayan R., 2013, A&A, 559, A116
Porth O., Olivares H., Mizuno Y., Younsi Z., Rezzolla L., Moscibrodzka M., Falcke H., Kramer M., 2017, Comput. Astrophys. Cosmol., 4, 1
Porth O. et al., 2019, ApJS, 243, 26
Porth O., Mizuno Y., Younsi Z., Fromm C. M., 2020, MNRAS, 502, 2023
Quataert E., Gruzinov A., 2000, ApJ, 539, 809
Ressler S. M., Tchekhovskoy A., Quataert E., Chandra M., Gammie C. F., 2015, MNRAS, 454, 1848
Ressler S. M., Quataert E., Stone J. M., 2018, MNRAS, 478, 3544
Ressler S. M., Quataert E., Stone J. M., 2020a, MNRAS, 492, 3272
Ressler S. M., White C. J., Quataert E., Stone J. M., 2020b, ApJ, 896, L6
Ricarte A., Prather B. S., Wong G. N., Narayan R., Gammie C., Johnson M. D., 2020, MNRAS, 498, 5468
Ripperda B. et al., 2019, ApJS, 244, 10
Royster M. J., Yusef-Zadeh F., Wardle M., Kunneriath D., Cotton W., Roberts D. A., 2019, ApJ, 872, 2
Russell H. R., Fabian A. C., McNamara B. R., Broderick A. E., 2015, MNRAS, 451, 588
Ryan B. R., Dolence J. C., Gammie C. F., 2015, ApJ, 807, 31
Ryan B. R., Ressler S. M., Dolence J. C., Tchekhovskoy A., Gammie C., Quataert E., 2017, ApJ, 844, L24
Shcherbakov R. V., Baganoff F. K., 2010, ApJ, 716, 504
Shvartsman V. F., 1971, Sov. Astron., 15, 377
Stone J. M., Tomida K., White C. J., Felker K. G., 2020, ApJS, 249, 4
Sądowski A., Wielgus M., Narayan R., Abarca D., McKinney J. C., Chael A., 2017, MNRAS, 466, 705
Tchekhovskoy A., Bromberg O., 2016, MNRAS, 461, L46
Tchekhovskoy A., Narayan R., McKinney J. C., 2011, MNRAS, 418, L79
Wald R. M., 1974, Phys. Rev. D, 10, 1680
Wang Q. D. et al., 2013, Science, 341, 981
White C. J., Stone J. M., Gammie C. F., 2016, ApJS, 225, 22
White C. J., Stone J. M., Quataert E., 2019a, ApJ, 874, 168
White C. J., Quataert E., Blaes O., 2019b, ApJ, 878, 51
White C. J., Dexter J., Blaes O., Quataert E., 2020, ApJ, 894, 14
Xu Y.-D., Narayan R., Quataert E., Yuan F., Baganoff F. K., 2006, ApJ, 640, 319
Yuan F., Quataert E., Narayan R., 2003, ApJ, 598, 301
Yusef-Zadeh F., Royster M., Wardle M., Cotton W., Kunneriath D., Heywood I., Michail J., 2020, MNRAS, 499, 3909

This paper has been typeset from a TeX/LaTeX file prepared by the author.